Exploration of the flow field around an oscillating sphere using 3D particle tracking velocimetry

Diplomarbeit
von
Florian Otto
aus
Straubing

Durchgeführt am
Institut für Experimentelle und Angewandte Physik
der Universität Regensburg
unter Anleitung von Prof. Dr. D. Göritz und Prof. Dr. W. Schoepe
und dem
Physics Department
der Wesleyan University, Middletown, USA
unter Anleitung von Prof. Dr. G. Voth

März 2004

For my parents

Contents

Chapter 1

Introduction

Self-organization processes with particles in a variety of sizes and systems have drawn the attention of researchers all over the world during the last decades. Apart from being a playground for fundamental research they are also of high relevance to some interesting applications in biophysics, material science and technical engineering. People have tried several different ways of producing the interaction necessary for the ordering, for example magnetized discs in a fluid in the field of a rotating permanent magnet([1], 2000), or pattern formation of colloidal particles due to electric fields ([2], 1997). Another experiment, which builds the basis for this thesis, reported "Ordered clusters and dynamical states of particles in a vibrated fluid" ([3], 2002). There, steel spheres of approximately 0.4 mm were suspended in a water/glycerol mixture and vibrated vertically with a shaker. This resulted in clustering and ordered crystalline patterns as well as dynamical fluctuating states, i.e. long range attraction and short range repulsion, which were shown to originate from fluid mediated interactions. The attractive part of the interactions could be modeled quantitatively with calculations of the streaming flow, whereas the repulsion could not be explained satisfactorily.
When a solid body oscillates in a viscous fluid, a steady streaming flow is produced. This has been know for quite some time (see for example [4], 1883 and [5], 1932). A good example of such a flow is the steady streaming due to an oscillating cylinder shown in figure 1.1, taken from "An album of fluid motion" by van Dyke (see [6]). The streaming (at these parameters) is divided up into a pumping directed from the center plane towards the axis of oscillation in the outer regions and smaller recirculating zones next to the cylinder with an opposite rotational direction. This steady streaming offers a possible explanation of both the attractive and repulsive interactions between particles observed in [3].
The flow field around an oscillating sphere shows basically the same structure, and thus the assumption of the inward pumping being responsible for the attraction observed in [3] seems to make good sense. As already said, the repulsive part of the interactions could not be explained as easily and was thought to originate from the inner recirculation zones, which should in general repel a second sphere coming close. But explaining the details of this repulsion was posed as a challenge for future work by that time.

So the idea of my experiment was to look explicitely at the flow field around an oscillating sphere and adress the following points:

- unperturbed flow field around a single oscillating sphere (without boundaries, i.e.

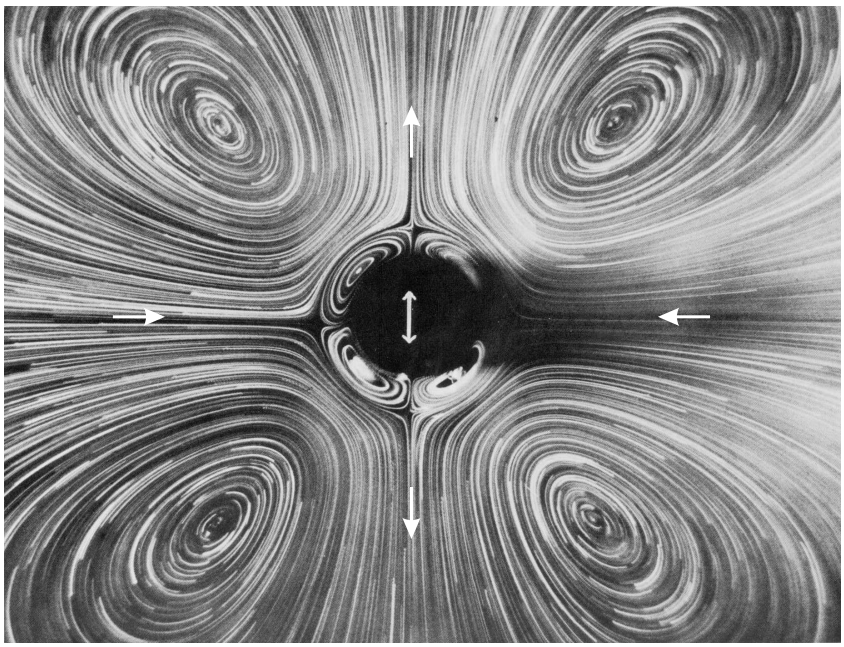

Figure 1.1: Secondary streaming induced by an oscillating cylinder at a Reynolds number of 140 [2] *and an amplitude of 0.17 times the radius of the cylinder (taken from 'An album of fluid motion' [6]).*

in the middle of a tank)

- changes to the flow field due to the presence of the bottom wall of the container (as the situation was in the experiments in [3])
- size and structure of the recirculation zones to indentify the source of the repulsion
- inflow velocities of the pumping flow

The technique we employed to get answers to the questions above was 'particle tracking velocimetry' (PTV), which uses high-speed digital camera equipment to follow the trajectories of small tracer particles over time and thus is able to extract velocities from basic principles. Our system had to be built from scratch, and consisted of two 1280x1024 digital cameras capable of taking up to 500 frames per second (fps) at full resolution. For my experiments, the frame rates usually did not exceed 100 fps (most of the time operating at even lower speeds at around 2-20 fps), but the cameras are also intended for use by other experiments in our lab, such as granular and turbulence experiments. By providing a stereoscopic view of the flow, our setup made it possible to get full 3-dimensional velocity fields. The whole setup as well as the experiment itself is also seen as a first step of the group towards a PTV system for the exploration of turbulence in the future[3]. While starting with an empty laboratory is a delightful task for an experimentalist, it also constitutes an enormous difficulty, especially if the time frame for the whole

[2] based upon the diameter of the cylinder and the frequency of oscillation

[3] hopefully with 3 or 4 cameras then

project is confined to 12 months, as is the case with a German 'Diplomarbeit'[4]. Among all the problems that have to be solved during the implementation of such a system are the calibration procedure of the cameras, critical for high precision measurements, the synchronization of the cameras, illumination and the choice of tracer particles, in our case also the construction of a driving mechanism for the sphere, building a tank and writing the computer programs for the analysis of the digital data. All of this could be accomplished, and our simple system already proved to work sufficiently well for the purpose of this thesis and thus builds a good starting point for the construction of the more complex turbulence experiments.

Regarding the origin of the repulsive interactions between particles in a vibrated fluid I will show that the explanations put forward so far are way too simple to account for the complex behavior seen in [3], especially that two (or more) particle effects have to be taken into account. Besides, I will demonstrate that the existing theories do not agree with the steady streaming flow that I have measured. They were derived for limits on oscillation amplitude and Reynolds number that appear to be too far from the experimental parameter regime for these theories to adequately describe my measurements or the flows in [3]. So in my view, theorists and experimentalists are yet to find a way to work in a regime of common parameters, since my experiments reveal significant discrepancies between the flows in our parameter regime and former theories as well as simulations.

[4]thesis as partial fulfillment of the requirements for the degree of a German Diplom, similar to a M.A.

Chapter 2

Theoretical Background

2.1 Steady streaming

A very general subfield of fluid dynamics is gathered under the term 'steady streaming', which contains all phenomena where the time-average of a fluctuating flow results in a nonzero mean. This may come directly from a nonconservative oscillatory body force or indirectly from a conservative one, which creates Reynolds stresses within the main body of the fluid or in thin boundary layers at no-slip boundaries. Although often used in this context, 'acoustic streaming' is not really an equivalent term, since many of the processes under consideration are taking place in incompressible fluids. Most of what will be said in this section is described in much greater detail in a recent (2001) review article by N. Riley [7]. I will just try to embed the special case of my experiment in a greater context.

Let me start by introducing the Navier-Stokes equations, which govern the dynamics of an incompressible fluid of constant viscosity:

$$\frac{\partial \vec{u'}}{\partial t'} + (\vec{u'} \cdot \nabla)\vec{u'} = -\frac{1}{\rho}\nabla p' + \frac{\eta}{\rho}\ \nabla^2 \vec{u'} + \vec{F'} \tag{2.1}$$

$$\nabla \cdot \vec{u'} = 0\ , \tag{2.2}$$

where ρ is the density of the fluid, $\vec{u'}$ the velocity field, p' the pressure, η the dynamic viscosity and $\vec{F'}$ a body force per unit mass. The second equation is known as 'continuity equation' and stands for the conservation of mass. Often, it is very convenient to introduce dimensionless variables, e.g.

$$\vec{x} := \vec{x'}/a\ , \qquad t := \omega t'\ , \qquad \vec{u} := \vec{u'}/u_0\ , \qquad p := p'/(\rho u_0^2), \qquad \vec{F} = \vec{F'}/F_0\ , \tag{2.3}$$

using typical values for all quantities (a: characteristic length, ω: frequency associated with the oscillatory body force, u_0: typical velocity, ρu_0^2: typical pressure, F_0: typical value of the applied force). This gives

$$u_0\omega\frac{\partial\vec{u}}{\partial t}+\frac{u_0^2}{a}(\vec{u}\cdot\nabla)\vec{u} = -\frac{1}{\rho}\frac{\rho u_0^2}{a}\nabla p+\frac{\eta u_0}{\rho a^2}\nabla^2\vec{u}+F_0\vec{F} \quad (2.4)$$

$$\frac{u_0}{a}\nabla\cdot\vec{u} = 0\ , \quad (2.5)$$

and after dividing the first equation by $(u_0\omega)$, the second by u_0/a, the nondimensional form of the Navier-Stokes equations looks like this:

$$\frac{\partial\vec{u}}{\partial t}+\varepsilon(\vec{u}\cdot\nabla)\vec{u} = -\varepsilon\nabla p+\frac{\varepsilon}{Re}\nabla^2\vec{u}+\frac{F_0}{u_0\omega}\vec{F} \quad (2.6)$$

$$\nabla\cdot\vec{u} = 0\ , \quad (2.7)$$

with the two characteristic dimensionless parameters being the Reynolds number $Re := u_0a/\nu$ ($\nu = \eta/\rho$ is called the kinematic viscosity) and $\varepsilon := u_0/(a\omega)$. The latter can be considered as the inverse of a Strouhal number, but is better understood as a non-dimensional amplitude in our case, since if the force is oscillatory (frequency ω), the velocity u_0 will be something like $A\omega$, where A is the amplitude of oscillation. The reason why this is important is given by a principle called 'dynamical similarity', which states that the physical properties of a system will be the same in geometrically similar situations. A more precise way of saying this is to gather all parameters that govern the behavior of a given system in their nondimensional combinations, and if then all of them are the same for two different flows, the physical properties should be the same as well. In our case, those governing parameters are given by Re and ε, in other cases there can be more or different ones, e.g. the Prandtl number $Pr := \nu/\chi$, if convection is important (χ being the thermal conductivity), or the Froude number $Fr := u^2/(ag)$, if gravity has to be taken into account. There are many more of course. The fact that most of them have special names also indicates that they are considered to be an important step towards understanding the behavior of a given flow.

One general restriction in most of the theoretical work done so far is that the amplitude A of oscillation is (nearly) always assumed to be small compared with the typical dimension a of the problem (e.g. in my case the radius of the sphere), or mathematically speaking, that

$$\varepsilon = \frac{u_0}{a\omega} = \frac{A}{a} \ll 1\ . \quad (2.8)$$

The general idea is to first calculate an 'unperturbed' leading order solution and then consider higher-order terms in ε.
One of the first people to address these kinds of problems was Lord Rayleigh in 1884, who examined standing sound waves between plane walls. Honouring his pioneering work, 'Rayleigh streaming' is the term given to flows with a relative oscillatory motion

between the fluid and a boundary. The main source for steady streaming in that case is viscous attenuation close to such a boundary or in the acoustic boundary layer. The second basic type of acoustic streaming is called 'Eckart streaming' or 'quartz wind', where in contrast the streaming results from viscous attenuation in the bulk of the fluid and any boundary effects are usually neglected [1]. Sometimes, 'quartz wind' also just describes steady streaming associated with an ultrasonic beam. If dealing with such acoustic streaming, the equations of motion have to be adjusted of course, since then the density is no longer a constant and the simple continuity equation (2.7) has to be modified:

$$\frac{\partial \rho}{\partial t} + \nabla \cdot (\rho \vec{u}) = 0 \ . \tag{2.9}$$

In his review article, Riley demonstrates where the steady streaming in a basic oscillatory flow induced by a conservative body force comes from. First he points out that at leading order and $Re \gg 1$, any such flow is irrotational without steady streaming, if no boundary effects are taken into account. But by considering the slip velocity at the boundary, it can be shown that higher-order terms include a fluctuating vorticity in the Stokes layer and that this gives rise to Reynolds stresses. These then create a steady streaming velocity that persists beyond the Stokes layer and drives the steady streaming in the bulk of the fluid. It also becomes clear that in that case a Reynolds number $R_s := \varepsilon \cdot Re$ is the governing parameter (instead of Re), since the velocity is smaller by a factor ε than when the body force is nonconservative.

There is a real plenitude of examples and wonderful experiments that belong to these types of flows. Not only have people looked at flows around oscillatory solid obstacles, like cylinders or spheres, but also at vibrating gaseous cavities or liquid droplets ([9, 10]), enhancement of heat transfer by the steady streaming about oscillatory particles ([11]) or acoustic levitation enhancing the growth of crystals ([12]). A recent (2003) example for these kinds of flows still being important even in a biophysical and technological context was given by Marmottant and Hilgenfeldt (see [13]), who investigated the 'controlled vesicle deformation and lysis by single oscillating bubbles'. Such a flow field, although created from the combination of bubble volume and translational oscillations, was presented to still be geometrically pretty similar to the flows around our solid sphere, and used to deform and finally rupture lipid membranes. This, according to the authors, promises to provide an interesting instrument for the further investigation and controlled manipulation of cells and maybe even future applications as 'acoustical tweezers' or the construction of microfluidic devices based on the same principles.

Again, it is way beyond the scope of this thesis to cover every single aspect of steady streaming, this section was really just meant to give a rough overview of the field.

[1] definitions from [8]

2.2 The flow-field around an oscillating sphere

In this section I will give a summary of what theorists predict for the special case of an oscillating sphere in a viscous fluid that is otherwise at rest. Unfortunately, there hasn't been a consistent theory so far that covers all aspects in different parameter regimes in a general way. One approach is to work in the limit of infinitesimal amplitude, assuming viscous steady flow outside an inner boundary layer, and I will summarize this method in the following subsections. My analysis closely follows [14] and [15]. A very general treatment of oscillatory motion in a viscous fluid is also given in the famous textbook "Hydrodynamics" by Landau & Lifschitz ([16]), part of their series in theoretical physics, but although working in the same limits, they do not give any detailed solutions on the velocity fields.

A different approach by Brenner and Stone (2002), which built the theoretical basis for the analysis in [3], assumes a potential flow far from the sphere, and I will give the results of their calculations at the end of this chapter as well.

The sphere of radius a shall have a velocity $u_{sphere} = A\omega\cos(\omega t)$ and again, the nondimensional amplitude $\varepsilon = A/a$ is assumed to be small throughout. As mentioned above, a steady streaming is then to be expected, and the details will now be discussed. The calculations had also been done earlier in the case of a cylinder (see for example [17, 18, 19, 20]), and although the situation changes a bit for a sphere, similar methods may be adopted. The starting point for this axisymmetric problem is given by equation 2.1 in spherical polar coordinates. Symmetry then tells us that there should be no motion in the azimuthal or φ-direction. So immediately, we are back at a fundamentally 2-dimensional problem. After non-dimensionalizing the equation the same way as above, applying the operator *curl* removes both the pressure and the body force, since any conservative force can be written as the (negative) gradient of a scalar potential, and thus we have *curl(grad)*, which is generally zero. The next step is the introduction of the stream function ψ, which is related to the (remaining) velocity components by

$$u_r := \frac{1}{r^2\sin\theta}\frac{\partial\psi}{\partial\theta} \quad , \qquad u_\theta := -\frac{1}{r\sin\theta}\frac{\partial\psi}{\partial r} \quad . \tag{2.10}$$

This can be seen from the continuity equation, which is then automatically fulfilled. The resulting new starting point is one equation for ψ:

$$|M|^2\frac{\partial(D^2\psi)}{\partial t} + \frac{Re}{r^2}\left(\frac{\partial(\psi, D^2\psi)}{\partial(r,\mu)} + 2D^2\psi L\psi\right) = D^4\psi \quad , \tag{2.11}$$

where

$$\begin{aligned} M^2 &:= \frac{i\omega a^2}{\nu} \quad , \\ \mu &:= \cos\theta \quad , \\ D^2 &:= \frac{\partial^2}{\partial r^2} + \frac{1-\mu^2}{r^2}\frac{\partial^2}{\partial\mu^2} \quad , \end{aligned}$$

$$L := \frac{\mu}{1-\mu^2}\frac{\partial}{\partial r} + \frac{1}{r}\frac{\partial}{\partial \mu} \ ,$$

and the boundary conditions are given by

$$\psi(r,\mu,t)\Big|_{r=1} = \frac{\partial \psi}{\partial r}\Big|_{r=1} = 0 \ , \tag{2.12}$$

$$\lim_{r\to\infty} \psi(r,\mu,t) \sim \frac{1}{2} r^2 (1-\mu^2) e^{it} \ . \tag{2.13}$$

As usual, the complex notation is used as a mathematical tool, and the physical significance is associated with the real part. The nondimensional parameters Re and $|M|^2$ used for this problem are defined by

$$Re := \frac{A\omega a}{\nu} \tag{2.14}$$

$$|M|^2 := \frac{\omega a^2}{\nu} \ . \tag{2.15}$$

As mentioned above, we will now first consider the leading order terms for a near and a far field solution and then, by use of a technique called 'matched asymptotic expansion', look at higher orders to improve the simple solution in special cases.

2.2.1 The first order solution

Equation (2.15) gives a relation between Re, $|M|^2$ and ε,

$$|M|^2 = \frac{Re}{\varepsilon} \ , \tag{2.16}$$

and tells us that the original restriction, $\varepsilon \ll 1$ can also be expressed as $|M|^2 \gg Re$. Thus to first order we can neglect the non-linear inertia terms in equation (2.11) and so if we call ψ_0 the first-order solution, we have

$$|M|^2 \frac{\partial (D^2 \psi_0)}{\partial t} = D^4 \psi_0 \ , \tag{2.17}$$

together with the boundary conditions (2.12) and (2.13). This problem can be found even in early textbooks ([21]) and yields

$$\psi_0(r,\mu,t) = \phi_0(r)(1-\mu^2)e^{it} \ , \tag{2.18}$$

with

$$\phi_0 = \frac{1}{2}r^2 - \left(\frac{M^2+3M+3}{2M^2}\right)\frac{1}{r} + \frac{3}{2M}\left(1+\frac{1}{Mr}\right)e^{M(1-r)} \ . \tag{2.19}$$

It can easily be shown that only the third term of (2.19) contributes to the creation of vorticity and that this vorticity diffuses over a region of extent $\mathcal{O}(|M|^{-1})$, the classical viscous penetration depth L_ν, as can be seen from

$$\frac{1}{|M|} = \frac{1}{\sqrt{\omega a^2/\nu}} = \frac{\sqrt{\nu/\omega}}{a} = \frac{L_\nu}{a} \ , \tag{2.20}$$

non-dimensionalized as before by our characteristic length, a. So our next natural step is to look at the two distinct cases

- $|M| \ll 1$, where the region over which the vorticity diffuses is large compared to a, and
- $|M| \gg 1$, where the first-order fluctuating vorticity is confined to a thin 'shear-wave' region next to the sphere.

2.2.2 First case: $|M|^2 \ll 1$

The headline of this subsection together with our original restriction for ε also requires that $Re \ll |M|^2 \ll 1$ (see equation (2.16)). The basic approach is

$$\psi = \psi_0 + Re\psi_1 + ... \ , \tag{2.21}$$

an ordinary perturbation expansion. Yet it has proven to be convenient to split this up into separate 'inner' and 'outer' solutions, which are then required to match to each single order and to be asymptotically correct in the limit as $Re \to 0$ ('matched asymptotic expansion'). The first order solution (2.18) for the inner region in this case is simply

$$\begin{aligned} \psi_0 &= \lim_{|M|\to 0}\left\{\frac{1}{2}r^2 - \left(\frac{M^2+3M+3}{2M^2}\right)\frac{1}{r} + \frac{3}{2M}\left(1+\frac{1}{Mr}\right)e^{M(1-r)}\right\}(1-\mu^2)e^{it} \\ &= \frac{1}{4}\left(2r^2 - 3r + \frac{1}{r}\right)(1-\mu^2)e^{it} + \mathcal{O}(|M|) \ . \end{aligned} \tag{2.22}$$

This is exactly Stoke's solution for steady flow past a sphere times the factor e^{it}, taking care of the low frequency fluctuations in our case. Next, the terms for ψ_1 are evaluated

and then the same (first Ψ_0, then Ψ_1) is done for the outer region, and by comparing the coefficients for each order, the two solutions are matched to give an overall solution. Since this is a rather longish procedure, I will skip the details and refer the reader to the original work ([14] and [15]). The final result is not very descriptive as a formula, but the author then also gives a flow pattern of the **steady streaming** (the nonzero time-averge flow) for this case, which is shown in figure 2.1.

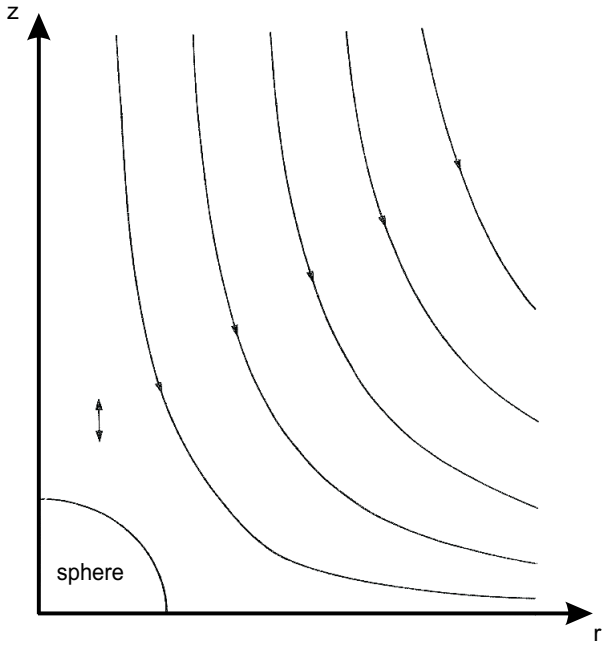

Figure 2.1: Streamlines of the theoretical steady flow prediction by Riley [14] in the regime where $|M|^2 \ll 1$. The sphere is centered around the origin and the direction of oscillation is given by $\longleftrightarrow$ (picture taken from [14]).

The resulting steady streaming is thus axisymmetrically directed away from the axis of oscillation towards the equator. This regime was very hard to get to in our experiment, since $Re \ll |M|^2 \ll 1$ basically means that not only would we have to work with very small amplitudes ($\varepsilon \ll 1$), but also with even smaller Re. This results in such small velocities that our setup mainly produces convection rolls or simply bouyancy drift, because the particles rise too fast for any steady streaming to occur before they leave the observation volume. Besides, the source for the streaming that (most likely) produced the patterns seen in [3], as described in the introduction, has to be of the second type in order to cause attraction. This will become clear in the next subsection.

2.2.3 Second case: $|M|^2 \gg 1$

Since $\varepsilon = Re/|M|^2$, our original restriction $\varepsilon \ll 1$ is fulfilled even without further conditions on Re. As already mentioned above, in the case under consideration, where $|M|^2 \gg 1$, the first order solution tells us that the vorticity is confined to a thin 'shear-wave' layer of $\mathcal{O}(|M|^{-1})$. The outer and inner first order solutions may thus be written as

$$\psi_0 \sim \left(\frac{1}{2}r^2 - \frac{1}{2r}\right)(1-\mu^2)e^{it} \tag{2.23}$$

and

$$\Psi_0 \sim \frac{3}{2}\left\{\eta - \left(\frac{1-i}{2}\right)(1-e^{-(1+i)\eta})\right\}(1-\mu^2)e^{it} \tag{2.24}$$

respectively (compare to equations (2.18) and (2.19)), where use of the following two definitions has been made:

$$\eta := (r-1)\frac{|M|}{\sqrt{2}} \ , \qquad \Psi := \frac{\sqrt{R_s}}{\varepsilon\sqrt{2}}\psi \ . \tag{2.25}$$

Now, we are looking for a perturbation solution of the form

$$\psi(r,\mu,t) = \psi_0(r,\mu,t) + \varepsilon\psi_1(r,\mu,t) + \mathcal{O}(\varepsilon^2) \tag{2.26}$$

After a considerable amount of manipulation and the use of former results for boundary layer equations and the 2-dim. case of the cylinder, a flow pattern for this case is also gained, shown in figure 2.2. It was already mentioned in the general steady streaming section that a Reynolds number based upon the velocity $\varepsilon\vec{u}$ becomes the governing nondimensional paramter in this case:

$$R_s := \varepsilon Re \ . \tag{2.27}$$

In the special case of $R_s \ll 1$, the solution can be written as

$$\psi = \psi_0 + \varepsilon(1-\mu^2)\left\{\frac{45}{32}\mu(1-\frac{1}{r^2}) - \frac{3}{2\sqrt{R_s}}\frac{1}{r}\cos(t-\frac{\pi}{4})\right\} \ , \tag{2.28}$$

with ψ_0 given by equation (2.23). The details of the calculation can be gleaned in [14] and [15]. This time, there is a thin boundary layer close to the sphere, beyond which steady streaming persists, but now axisymmetrically directed towards the axis of oscillation, away from the equator.
Similar flow patterns have been reported in [22], shown in figure 2.3.

This theoretical result for a single sphere pretty obviously provides a qualitative explanation for the attraction reported in [3], and guesses have been made that the repulsion observed between particles in an oscillatory liquid environment may be connected to the inner recirculation zones, but the details give rise to some further questions and problems.

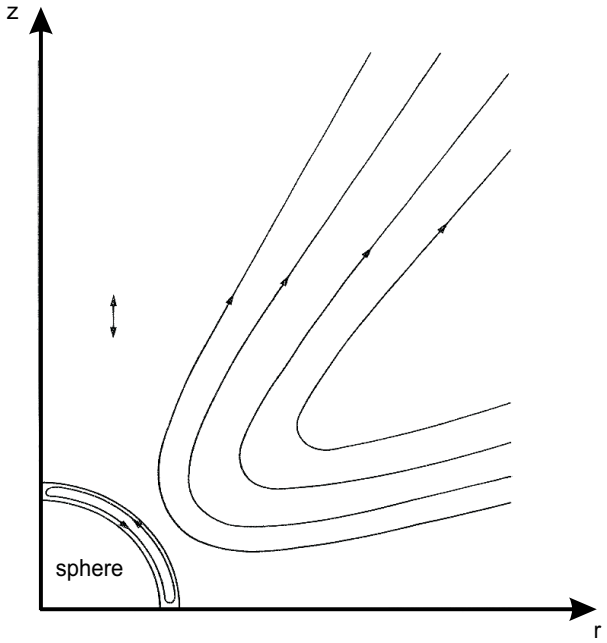

Figure 2.2: Streamlines of the theoretical steady flow prediction by Riley [14] in the regime where $|M|^2 \gg 1$, $R_s \ll 1$. Next to the sphere (centered around the origin) a closed loop within the shear-wave layer is shown (picture taken from [14]).

Another approach to the whole problem, which I mentioned at the beginning of this section, would be to assume that $R_s \gg 1$, leading to a potential flow everywhere outside the viscous boundary layer. This was actually done in [3] by Brenner and Stone to get the far field velocity in the high Reynolds number regime. Here, I just want to give the final result of this calculation:

$$u_r(r, \theta = 90°) = -0.53A\sqrt{\omega\nu}a^2\frac{1}{r^3} \quad , \tag{2.29}$$

where u_r is the radial velocity component at a distance r from the center of the sphere (valid for the far-field only). The negative sign stands for the fact that this velocity is the steady streaming **towards** the sphere along the equator ($\theta = 90°$), in other words the 'pumping', responsible for the attraction seen in [3].
In striking contrast to this formula, the first analysis outlined in detail above yields a far-field velocity

$$u_r(r, \theta = 90°) = -\frac{45}{32}\frac{\varepsilon}{r^2}\left(1 - \frac{1}{r^2}\right) \quad , \tag{2.30}$$

using the relations

$$u_r := \frac{1}{r^2 \sin\theta}\frac{\partial\psi}{\partial\theta} \quad , \qquad u_\theta := -\frac{1}{r\sin\theta}\frac{\partial\psi}{\partial r} \tag{2.31}$$

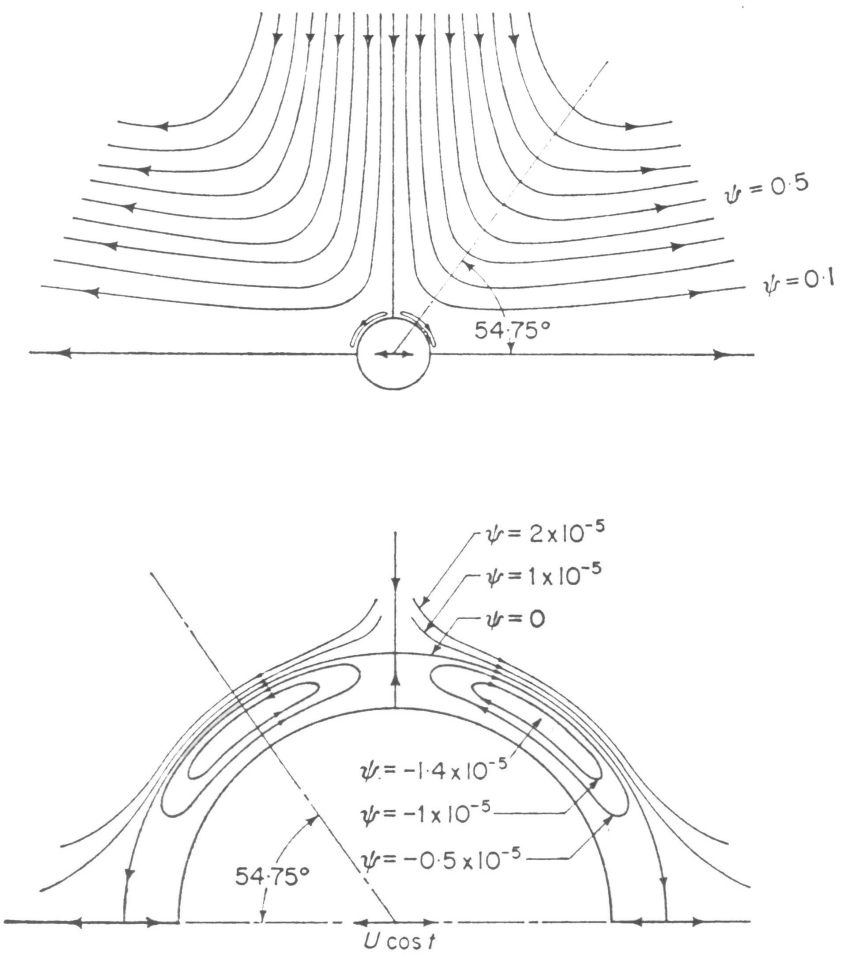

Figure 2.3: Streamlines of the theoretical steady flow prediction by Wang [22] for $\frac{1}{\varepsilon} = 90$, $Re = 80$. *The upper plot shows the whole field, whereas in the lower one, the boundary layer has been magnified 6 times. In both cases the axis of oscillation is horizontal (pictures taken from [22]).*

and equation (2.28). There has also been a recent numerical simulation by Blackburn (2002, [23]), which will be compared to the two theories in the results chapter, and unfortunately all three disagree significantly even in the limit of small ε. As far as it is understood up to now[2], it seems as if both theories give two different results consistently correct in their own limits, but the experiment should lie somewhere in between (even in the limit of infinitesimal amplitude!). Additionally, our experiment typically had to be conducted with rather large amplitudes, and it seems that also the viscous effects on the steady flow can not be fully ignored in our Reynolds number range. In any case, there are the two theoretical results on the one hand, and my experiments on the other hand,

[2]communication with Prof. M. Brenner, brenner@deas.harvard.edu

and I will make the comparison in the results chapter.

Chapter 3

The experiment

3.1 A powerful technique: particle tracking velocimetry

During the last few decades, researchers all over the world have made considerable progress in trying to visualize and measure the velocities of flows of all kinds by the use of videogrammetric methods, i.e. making measurements from (video) images. Two of the most commonly used representatives are PTV (='particle tracking velocimetry') and PIV (='particle image velocimetry'), both of which image the displacement of tracer particles over short time intervals (consecutive video frames) and calculate their velocities with the help of the basic definition of velocity

$$\vec{u} := \lim_{\Delta t \to 0} \frac{\Delta \vec{x}}{\Delta t} \quad . \tag{3.1}$$

According to Dracos (1996,[24]), the latter seeks for 'the mean displacement of a small *group* of particles', whereas PTV 'tracks the trajectories of *individual* particles in three-dimensional space'. Another difference is the illumination of only a thin, two-dimensional sheet in PIV in contrast to the possibility of imaging a whole three-dimenensional volume with PTV. So although PIV would work (almost) just as well for the resolution of the flow field around a single sphere, the case of 2 spheres creating a full three-dimensional flow makes PTV the better choice for our experiments. In addition, the system we have built is a first step towards particle tracking in turbulent flows, which will be the next project of the group. Disadvantages of PTV are the requirement of a low particle number density and the restriction to low-speed flows due to the limited imaging frequency.
In a situation where one wants to examine a full 3-dimensional flow rather than a 2-dimensional one (which is usually the case with PTV), at least 2 cameras are necessary, since each camera will only produce a 2-dimensional view of the process. The advantage of this stereoscopic view of the motion also adds a separate problem: corresponding particles in the different views have to be matched. Thus, there are two possibilities to end up with particle trajectories and the velocities (see figure 3.1):

(i) follow the tracers through the 2-dimensional pictures of each camera separately and match their tracks afterwards, or

(ii) match the particles in each camera view for each frame first and then follow them through in 3-dimensional space.

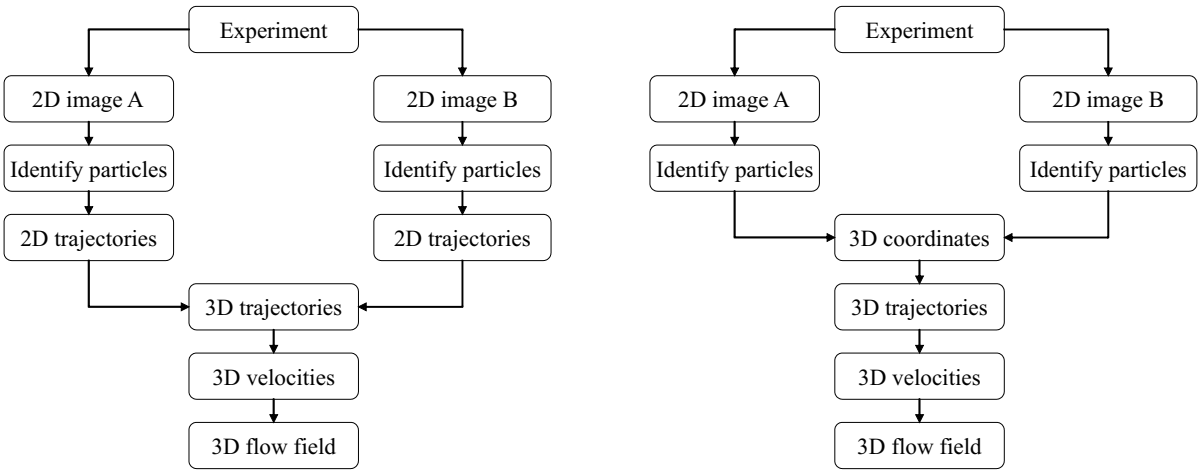

Figure 3.1: Two ways to analyze 3D PTV-data

The problem with the first one is that in 2D, particle tracks can (and in fact very often do) intersect, leading to confusion about which particle goes with which track. This experiment uses the second method, since some codes for the basic data processing already existed for it. But with only 2 cameras, a similar problem occurs: no matter how one sets them up, 2 cameras will only be able to distinguish particles that aren't hidden in one view. That is the reason for most people using three or even four cameras to avoid these ambiguities.
The principle of two-dimensional tracking is shown in figure 3.2 on the left. The most probable path of a given particle is determined by minimization of the difference between its estimated and real position. The basic idea of matching corresponding particles from different views is illustrated on the right, figure 3.2: each particle together with its image defines an optical ray, and thus two (or more) different views provide the information about the three-dimensional position of the particle by their (near) intersection.

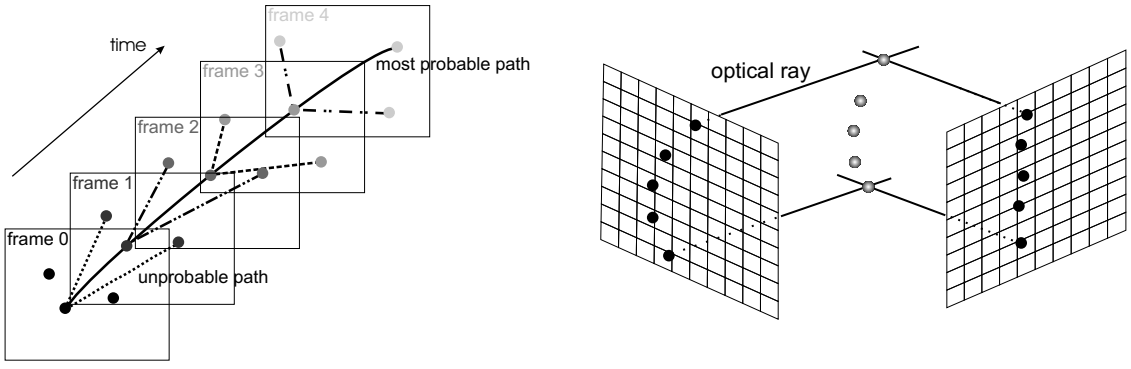

Figure 3.2: **(left)** *Principle of two-dimensional tracking.* **(right)** *Optical rays used for matching corresponding particles in different views*[2].

[2]both drawings as in Dracos (1996,[24], p.157)

The latter step, matching particles, calls for a mathematical model of the geometrical situation to determine 3-dimensional particle positions out of a pair of 2-dimensional images. This will be described in detail in the next subsection. For an extensive characterization of particle tracking techniques and their implementation, the reader is referred to [24] and [25].

3.1.1 Mathematical model

The mathematical model has two separate steps on its way towards giving the three-dimensional coordinates of a tracer particle: First, the optical rays on which one has to look for the particle have to be calculated from the information given by the calibration and the two-dimensional images. Then, these rays have to be matched by calculating the distance between all pairs of lines in both views (see figure 3.3 for illustration).

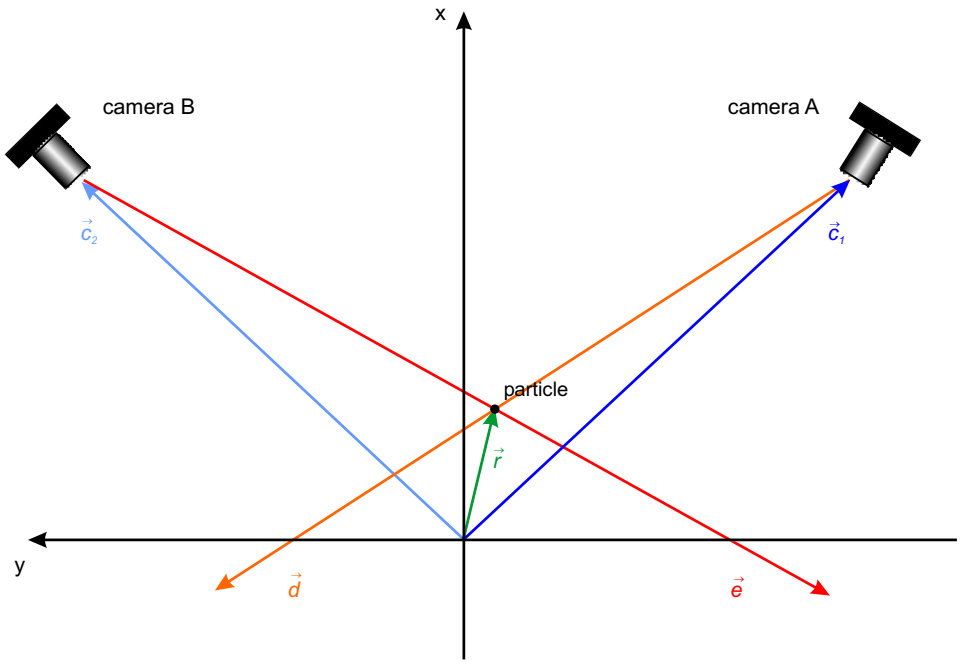

Figure 3.3: Optical-rays: The only information from the two 2-dimensional images are two 3-dimensional optical rays, whose (near) intersection defines the real-space position of a given particle.

Although much more complicated models have been developed (see [24, 25]), our simple (first) approach proved to work sufficiently well for our purposes. First of all, there are several approximations in our model:

- Both cameras (including lenses) are treated equally (there has been no testing of differences in their properties)

- Each camera is assumed to work like a pinhole, meaning the finite aperture and thick lenses are being neglected (but we do of course have a finite depth of focus)

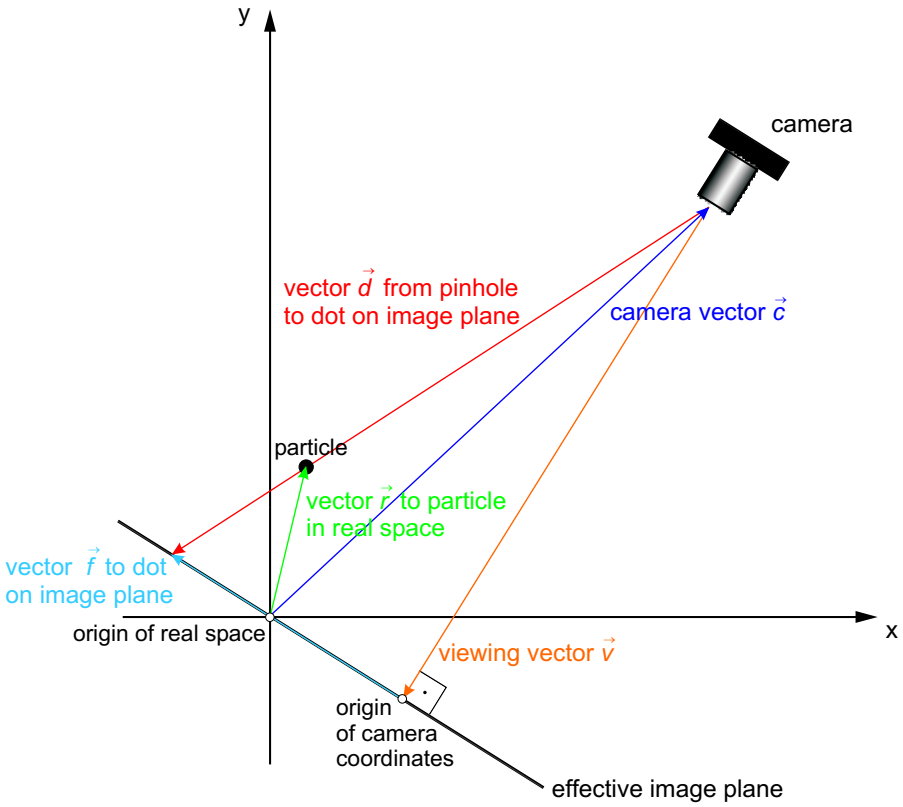

Figure 3.4: Definition of the vectors used to calculate the optical ray for each image of a particle.

- The effects of differences in indeces of refraction are only compensated for by the calibration, not by the mathematical procedure (our optical rays are assumed to be effectively straight lines)

Figure 3.4 shows a simplified version of the geometrical situation: the ray we are looking for is given by the vector $\vec{d}$ ($\vec{e}$ for camera B), i.e. the projection of the particle onto the (effective) image plane. Since we don't know that vector, we have to calculate its direction from the only information we have: the two-dimensional image and thus the vector $\vec{f}$ ($\vec{g}$ for camera B), given by the vertical and horizontal position of the bright spot on the CMOS-chip. So, in a sense, we have to go 'backwards':

$$\vec{d} = \vec{v} + \vec{f} \ . \tag{3.2}$$

Then, in a second step, we will calculate the distance between optical rays from the two camera views and thus try to match corresponding particles.

There are 2 more parameters not shown in the simple diagram: indepently of the viewing direction, the cameras can (and in general will) also be (slightly) rotated, meaning the vertical axis of the CMOS-array is not necessarily in the same direction for both cameras or parallel to the z-axis of the real-space coordinate system. The second one is the magnification, simply given by the ratio of distances in the camera plane measured

in pixels and actual distances in the camera plane. Those two together with the camera vector $\vec{c}$ and viewing vector $\vec{v}$ are determined by the calibration procedure (see section 3.4).

I will now describe in detail the first step of the mathematical procedure, which is finding the optical ray for each image of a particle. First of all, the 2-dimensional pixel-coordinates of the features found in both images get read in and those vectors are first called $\vec{f'}$ and $\vec{g'}$ for camera A and B respectively. Then, they get multiplied by the magnification factor γ and rotated by the rotation angle α (for camera A, β for camera B),

$$\vec{f} = \begin{pmatrix} \cos\alpha & \sin\alpha \\ -\sin\alpha & \cos\alpha \end{pmatrix} \begin{pmatrix} \gamma \cdot f_x{}' \\ \gamma \cdot f_y{}' \end{pmatrix} = \begin{pmatrix} f_x \\ f_y \end{pmatrix} \ . \tag{3.3}$$

In order to make the connection to 3D vectors, one has to realize that these 2D 'horizontal' and 'vertical' coordinates within the images are given naturally in real-space by spherical polar coordinates, with respect to the pinhole. Figure 3.5 shows the situation: here, the coordinates have been chosen as $\vec{r} = (r, \varphi, \theta)$, where φ is the azimuthal angle within the xy-plane, and θ gets measured down from the z-axis. Thus the local 2D coordinates on the image plane are given by the unit vectors $\hat{e_\varphi}$ and $\hat{e_\theta}$. But since these are rotated by 180° with respect to 'normal' x and y coordinates on a 2D-plane (meaning the way we usually interpret 2D coordinates, like in this case pixel positions; see figure 3.5), π gets added onto the rotation angle α (β). And so it makes sense to think of the 'new', rotated vector $\vec{f}$ ($\vec{g}$) like this:

$$\vec{f} = \begin{pmatrix} f_x \\ f_y \end{pmatrix} = f_x \hat{e_\varphi} + f_y \hat{e_\theta} \ . \tag{3.4}$$

The next step is a standard coordinate transformation (see [26]), which helps us to substitute $\hat{e_\varphi}$ and $\hat{e_\theta}$, in order to work in cartesian coordinates again:

$$\hat{e_\varphi} = \frac{-y\hat{e_x} + x\hat{e_y}}{\sqrt{x^2+y^2}} \tag{3.5}$$

$$\hat{e_\theta} = \frac{z(x\hat{e_x} + y\hat{e_y}) - (x^2+y^2)\hat{e_z}}{\sqrt{x^2+y^2}\sqrt{x^2+y^2+z^2}} \ . \tag{3.6}$$

So now we are able to write down a representation for the two optical rays (one for each camera, see figure 3.3), whose 'intersection' will provide us with the 3D position of a given particle. Due to measurement errors and inaccuracies they will of course never really intersect, but be close enough for us to identify and match features. The two optical rays are given by $\vec{d}$ and $\vec{e}$ through the following formula:

$$\begin{aligned} \vec{d} &= \vec{v_1} + f_x\hat{e_\varphi} + f_y\hat{e_\theta} = \\ &= \vec{v_1} + \left(\frac{-v_{1y}f_x}{\sqrt{v_{1x}^2+v_{1y}^2}} + \frac{v_{1z}v_{1x}f_y}{\sqrt{v_{1x}^2+v_{1y}^2}\sqrt{v_{1x}^2+v_{1y}^2+v_{1z}^2}}\right)\hat{e_x} \\ &\quad + \left(\frac{v_{1x}f_x}{\sqrt{v_{1x}^2+v_{1y}^2}} + \frac{v_{1z}v_{1y}f_y}{\sqrt{v_{1x}^2+v_{1y}^2}\sqrt{v_{1x}^2+v_{1y}^2+v_{1z}^2}}\right)\hat{e_y} \end{aligned}$$

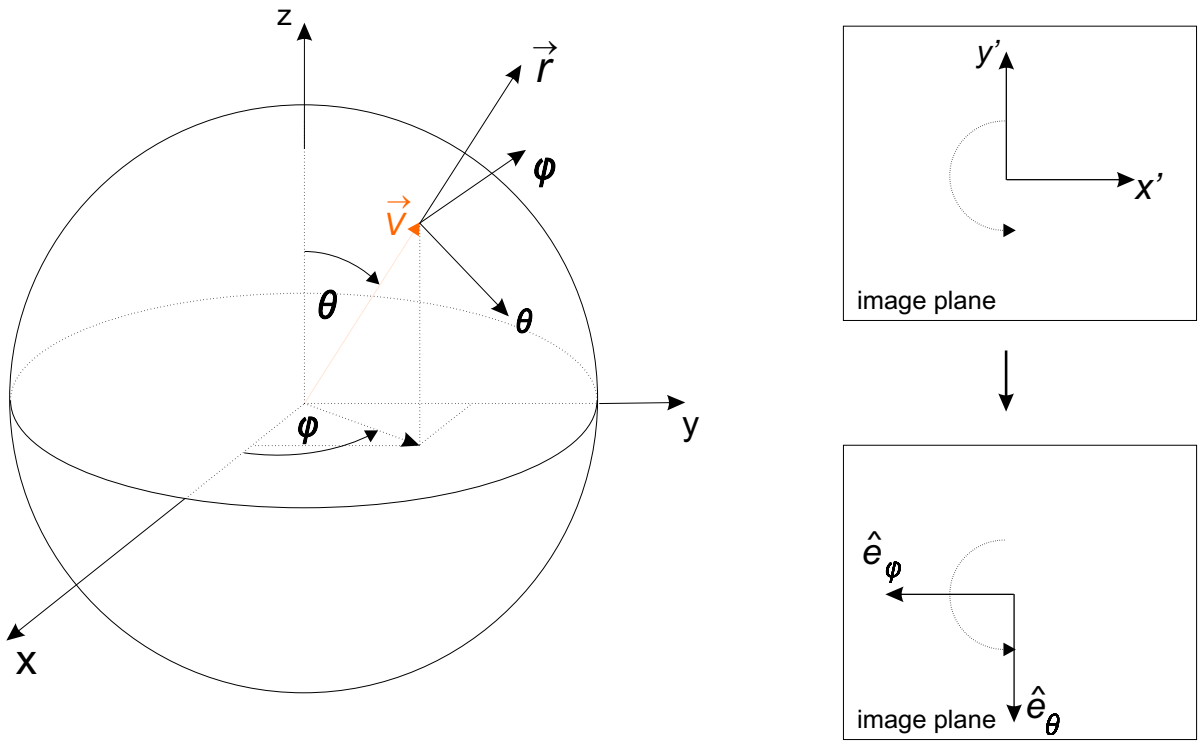

Figure 3.5: Definition of the spherical coordinates used (left), and illustration of the rotation necessary for using $\hat{e_\varphi}$ and $\hat{e_\theta}$ within the image plane

$$-\sqrt{\frac{v_{1x}^2+v_{1y}^2}{v_{1x}^2+v_{1y}^2+v_{1z}^2}}f_y\hat{e_z} \tag{3.7}$$

(for $\vec{e}$ (camera B), replace the $\vec{f}$-components with the $\vec{g}$ ones). So there should be two skew lines for each particle and the procedure then is to determine the distance between each skew line (optical ray) for each feature found in one image and each skew line in the other image. But the problem is that we do not only deal with one particle, but approx. 200, and thus there are many skew lines. Hopefully, our calibration and the setup will be good enough to still tell us which feature goes with which in the two images. Pairs of 'closest' skew lines will then define particle positions. The equations for the two rays are

$$\text{(camera A)} \quad g1: \quad \vec{c_1}+\lambda\vec{d} \tag{3.8}$$
$$\text{(camera B)} \quad g2: \quad \vec{c_2}+\mu\vec{e}\ . \tag{3.9}$$

In order to calculate the distance between those two lines, we define a plane

$$E: \vec{c_1}+\lambda\vec{d}+\mu\vec{e}\ , \tag{3.10}$$

which contains g_1 and is parallel to g_2. The normal vector of E is given by

$$\vec{n} := \frac{\vec{e}\times\vec{d}}{|\vec{e}\times\vec{d}|}\ . \tag{3.11}$$

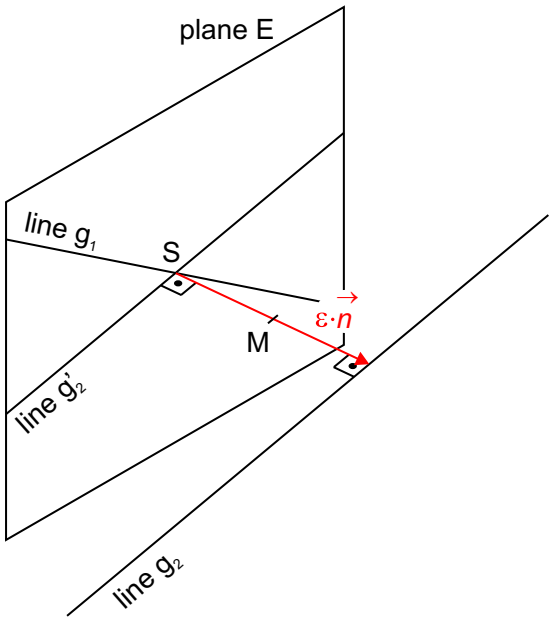

Figure 3.6: Skew lines: The distance ε between the two optical rays, g_1 and g_2, is calculated by intersecting g_1 and g_2' at S, where g_2 is the parallel to g_2 within the plane E, and then finding the center M of the connection line, given by $\varepsilon \cdot \vec{n}$, $\vec{n}$ being the normal vector of E.

What we are looking for is not only the distance (here called ε) between E and g_2, but also the coordinates of the center of the shortest connection line between g_1 and g_2, which will be used to define the particle position. That can be done by calculating the point of intersection of g_1 and g_2', the line that is parallel to g_2 and also lies in the plane E ($g_2' \in E$):

$$g_2' : \vec{c_2} + \mu\vec{e} - \varepsilon\vec{n} \ . \tag{3.12}$$

An illustration of this is given by figure 3.6[3]. So, once we have the distance ε, the best approximation for the particle position is given by

$$\vec{m} := \vec{s} + \frac{1}{2}\varepsilon\vec{n} \ , \tag{3.13}$$

where S is the point of intersection of g_1 and g_2' in E (see figures 3.3 and 3.6),

$$\vec{s} := \vec{c_1} + \lambda\vec{d} \ . \tag{3.14}$$

In order to get S, we have to solve the linear system of equations for $g_1 \cap g_2'$:

$$\vec{c_1} + \lambda\vec{d} = \vec{c_2} + \mu\vec{e} - \varepsilon\vec{n} \ , \tag{3.15}$$

[3]Note: the sign of $\varepsilon\vec{n}$ depends on the direction of $\vec{n}$ and is determined automatically by solving the linear system of equations below. Here it was chosen to be negative to better match the drawing.

or in components:

$$
\begin{aligned}
c_{2x} + \mu d_x + \varepsilon n_x &= c_{1x} + \lambda e_x && (3.16)\\
c_{2y} + \mu d_y + \varepsilon n_y &= c_{1y} + \lambda e_y && (3.17)\\
c_{2z} + \mu d_z + \varepsilon n_z &= c_{1z} + \lambda e_z \ . && (3.18)
\end{aligned}
$$

A solution for this (calculated by hand and mathematica) is

$$
\begin{aligned}
\mu &= -(c_{1z}e_y n_x - c_{2z}e_y n_x - c_{1y}e_z n_x + c_{2y}e_z n_x - c_{1z}e_x n_y + c_{2z}e_x n_y + c_{1x}e_z n_y - \\
&\quad c_{2x}e_z n_y + c_{1y}e_x n_z - c_{2y}e_x n_z - c_{1x}e_y n_z + c_{2x}e_y n_z)/ \\
&\quad (-d_z e_y n_x + d_y e_z n_x + d_z e_x n_y - d_x e_z n_y - d_y e_x n_z + d_x e_y n_z) && (3.19)\\
\varepsilon &= -(-c_{1z}d_y e_x + c_{2z}d_y e_x + c_{1y}d_z e_x - c_{2y}d_z e_x + c_{1z}d_x e_y - c_{2z}d_x e_y - c_{1x}d_z e_y + \\
&\quad c_{2x}d_z e_y - c_{1y}d_x e_z + c_{2y}d_x e_z + c_{1x}d_y e_z - c_{2x}d_y e_z)/(d_z e_y n_x - d_y e_z n_x - d_z e_x n_y + \\
&\quad d_x e_z n_y + d_y e_x n_z - d_x e_y n_z) && (3.20)\\
\lambda &= -(c_{1z}d_y n_x - c_{2z}d_y n_x - c_{1y}d_z n_x + c_{2y}d_z n_x - c_{1z}d_x n_y + c_{2z}d_x n_y + c_{1x}d_z n_y - \\
&\quad c_{2x}d_z n_y + c_{1y}d_x n_z - c_{2y}d_x n_z - c_{1x}d_y n_z + c_{2x}d_y n_z)/(-d_z e_y n_x + d_y e_z n_x + \\
&\quad d_z e_x n_y - d_x e_z n_y - d_y e_x n_z + d_x e_y n_z) \ . && (3.21)
\end{aligned}
$$

So now we have all we need mathematically to determine where a particle sits in real-space. But as mentioned above, there is not only one but approx. 200 features in each image. For still finding the right matches we calculate the distances between all the lines[4], and end up with a $n_1 \times n_2$ matrix (n_1, n_2: number of features found in each image), that contains all of those epsilons. If an ε then is the smallest value regarding the column **and** the row it lives in, **and** if it is smaller than a certain acceptance threshold, it is called a match. Thus we have the real-space position of the particles, given by the appropriate $\vec{m}$-vectors.

Although this simple model worked sufficiently well for our purposes, it also has its limitations. Since we only have two cameras (sitting approx. in the xy-plane), we cannot distinguish particles that are at the same height z: we only know the direction where we have to look for them in real-space, given by the optical rays, but not the depth or distance away from the camera. This is the major limitation to our experiment, namely that we can only use a medium particle number density of about 200 particles[5]. But this problem could be eliminated at once if one were to use three or four cameras, improving the accuracy of correct particle matching significantly. Here, we could not afford more cameras, since each costs about 30,000 $, but we do plan to get two more cameras eventually for imaging turbulent flows in the future. Another weakness of our simple mathematical model is the neglect of optical distortions and aberrations, as the assumption of exclusively straight rays is of course not true, but again, for our purposes worked well.

[4] in fact we only compare lines that live at approximately the same height z in real-space, since the two cameras are roughly aligned in that regard, and thus save computation time

[5] Having only two cameras, a lower particle density (e.g. 50-100) would give less mismatches on the one hand, but on the other hand a lot more data would be needed.

3.2 General setup

Schematic overviews of the setup are shown in figures 3.7 (left; top view) and 3.8 (side view). The sphere sits in the middle of an octagonal tank made out of plexiglas. The tank has an inner diameter of 30 cm, a height of about 25 cm and the wall thickness is 1.27 cm (=1/2 inch). The octagonal shape was chosen because it has nearly cylindrical symmetry, but still provides eight flat walls that make it easy to illuminate and observe. It is filled with a mixture of glycerol and water, adjusted to give the required viscosity. The cameras are set up at roughly 90° for the stereoscopic view. Three 750 Watts theater lights are placed at 45° and 135° with respect to each camera to get a symmetric illumination with less shadows than one would have with only one light source. The lights are running continously during the experiment, which causes one of the most significant problems we encountered, namely quite big convection rolls inside the tank[6]. On the other hand, the huge power of the lights is necessary for taking the fast video data at exposure times between 4 and 10 ms.

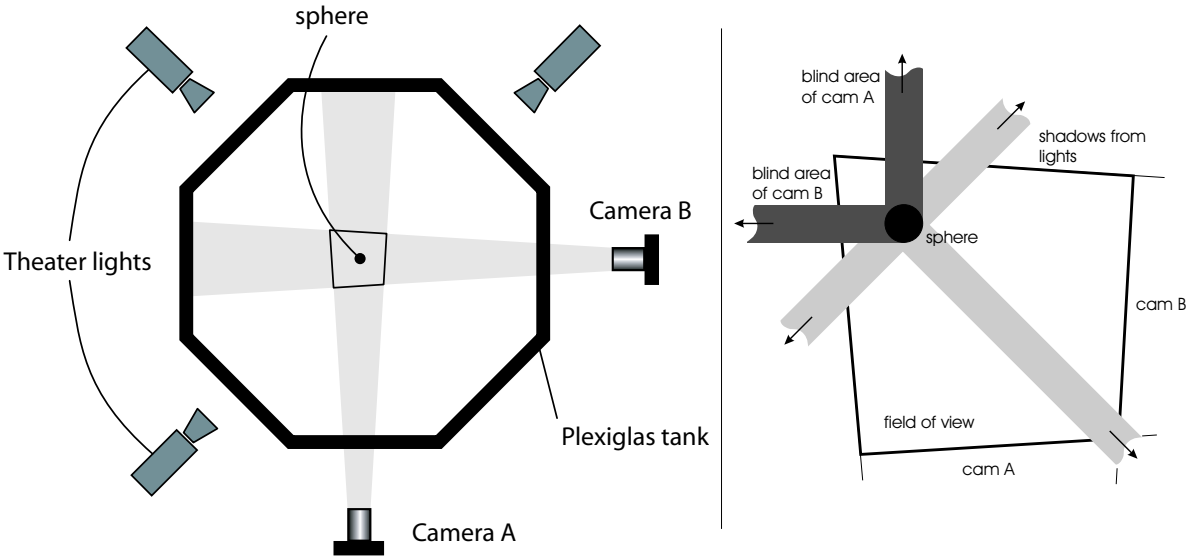

Figure 3.7: A top view of the setup: **(left)** *Three theater-lights provide symmetric illumination for both cameras observing at* 90°*, thus enabling stereoscopic imaging. In the middle of the tank, the overlap of the two fields of view around the sphere and* **(right)** *the shadows of the lights and the blind areas of the cameras are shown (zoomed in).*

Since there are only two cameras, there is one conical region 'behind' the sphere that is inaccessible for each of the cameras, which suggests to really move the field of view slightly 'in front of' the sphere (with respect to the cameras) as shown in the enlarged drawing in figure 3.7 on the right. Additionally, there are the three conical shadows caused by the sphere and each light (i.e. regions of less illumination, namely only two instead of three theater lights).
The driving mechanism is shown in figure 3.8: The shaft holding the sphere slides on a linear rail and is eccentrically connected to a circular disk, which itself sits on a stepper

[6]These problems are also discussed in appendix A

motor. The circular motion of the wheel is thus generating the desired up-and-down oscillations of the sphere. The vertical position of the sphere in the tank as well as the amplitude of the stroke can be adjusted continously by hand, and be measured in the video data with very good precision. At the heart of the experimental setup there are two 1.3 Megapixel high-speed cameras with CMOS-sensors. A summary of their features is given in table 3.1. They are capable of taking up to 500 frames per second at full resolution (1280x1024) or up to 16,000 frames per second at reduced resolutions (1280x32). Each of them has its own PC with 4 GB of RAM on a frame grabber card. This leads to a technical restriction of the camera system, since they can only take as many images at once as fit on their frame grabber memories, before the computers have to be given a pause, in which they can download the 4 GB from the frame grabber memory to the hard-disks. This is what will be referred to as one 'sequence' from now on, meaning the maximum number of images that can be taken without a pause, usually creating one data-set for a given set of parameters. Since the cameras operate at 8-bit grayscale, one image at full resolution (1280x1024) is approximately 1.2 MB, leading to a total of about 3200 images per sequence. The images then get stored on the hard-disks, a 600 GB raid-array in each PC.

The digital cameras use standard SLR-lenses (F-mount), which makes it possible to choose from the great variety of off-the-shelf photo-store lenses. We used two different kinds, 105 mm Macro-lenses (1:2,8) for our standard field of view and 28-135 Zoom lenses (1:3.8-5.6) for zooming in.

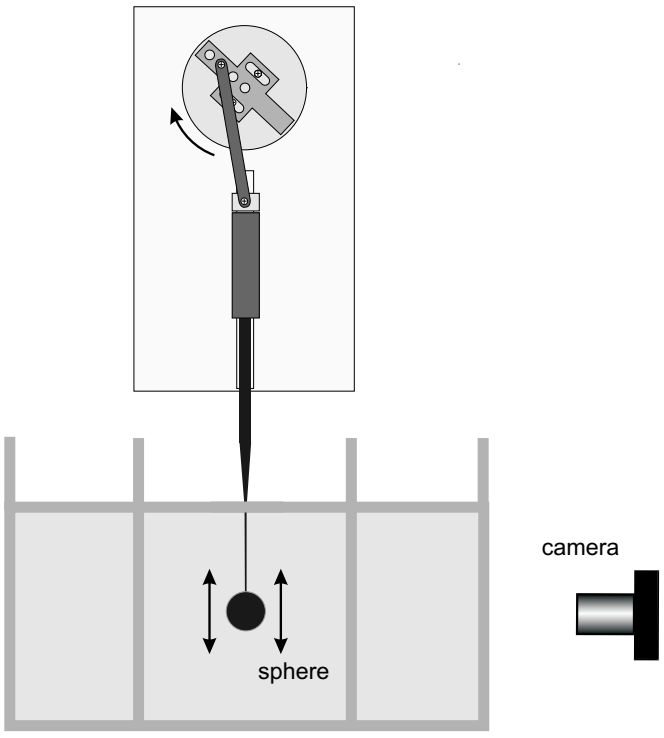

Figure 3.8: A side view of the setup. The circular motion of the disk sitting on a stepper-motor is converted to a linear up-and-down one by the use of an eccentric rod (similar to a steam train).

spec.	Basler A504k	spec.	Basler A504k
sensor size	1280 x 1024	sync.	ext. trigger or freerun
sensor type	CMOS	max. frame rate	500 fps
pixel size (μm)	12.0 x 12.0	lens mount	F-mount
pixel clock	67 Mhz	housing size (mm)	41.5 x 90 x 90

Table 3.1: camera specifications

3.3 Details of setup

3.3.1 Synchronization of the cameras

One of the most crucial things for this experiment is, of course, to be able to trigger the cameras, such that they take their images completely synchronized with each other **and** the motion of the sphere. Obviously, the two 2-dimensional images used for reconstructing the 3-dimensional position of particles have to be taken at the same time, otherwise the particles in, say image A will have moved with respect to the particles in image B, and there is no common position in real-space for most of them. Also, for analyzing the 'movies', it is more than natural to take the images at a fixed frequency, as this will define the time steps between successive images or Δt, which is needed for finding the velocities.

But why do they have to be synchronized with the motor, i.e. the motion of the sphere? Well, the answer is that the sphere is oscillating, and thus the position of the sphere and the direction it is moving in do matter: in order to get a stationary flow field (steady streaming = nonzero time-average), one has to look at the process in a frame of reference in which the sphere doesn't move. A reasonable thing to do is to look at periodic displacements over one period, i.e. to make the time interval between successive images a factor of the period of the oscillation of the sphere (it would also work with any given pair of time intervals, the 'period' of that process would then just be given by the least common multiple of the two; but that is not a very practicable solution). One can then look at sets of images at a common phase, so that the sphere is in fact not moving in successive images. And even if one wants to examine the non-stationary trajectories of single particles due to a moving sphere, it is also more convenient to 'know, where the sphere is', i.e. choose a frequency for taking the images that is synchronized with the period of oscillation. More about the different methods to interpret the 'movies' will be given in subsection 3.5.

In our experiment, we chose the following method for the camera-to-motor-synchronization: The disk that sits on the stepper motor (see figure 3.8) has 16 little holes near the edge, all of which are $22,5°$ apart, dividing the oscillation up into 16 different phases. There are two more holes at 90°, defining the middle and the uppermost (downmost) position of the stroke. The trigger signal for this synchronisation process is given by a laser beam, aligned such that everytime a hole on the turning wheel comes by a photodiode sitting behind the disk, the laser beam passes through and hits the photodiode, generating the signal (see figure 3.9). So depending on how many and which holes would be opened, we could choose the number of phases from 1 to 16.

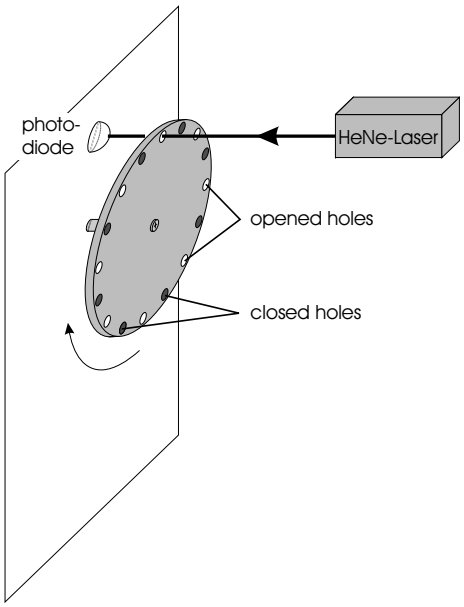

Figure 3.9: Synchronisatin of the cameras with the motor by the use of a signal generated by a laser-beam, hitting a photo-diode everytime one hole of a given set of opened holes crosses its way. The disk shown is eccentrically connected to the shaft that holds the sphere (see figure 3.8).

The trigger circuit is shown in appendix D and mainly consists of an amplified signal put into a Schmidt Trigger, and depending of the status of the 'reset' and 'trigger' buttons is amplified again with a line-driver and put through to the cameras.

3.3.2 Experimental difficulties and problems

The setup described above (section 3.2) has several weaknesses that result in restrictions regarding the access of the full phase space of our problem. In detail, the restrictions arise from the following:

(i) **Rod-effects** - One general problem is hard to evade: the sphere has to be supported or attached to some driving mechanism, and whatever one uses for this will influence the flow field (having the sphere bounce of the shaken bottom plate as in [3] does not seem to be a very efficient way for PTV, as one would have to not only trace the tracer particles but also the sphere and calculate their relative positions in an extra step; some kind of a electromagnetic shaker with a dielectric sphere constitutes the problem of rather small dimensions for the whole setup, which has the disadvantage of smaller particles scattering even less light at higher speeds). Measurements of this disturbance will be presented in section 4.1.1.

(ii) **Heat** - The theater lights we used each had about 750 Watts, and this continous input of heat into the tank caused considerable convection in the fluid, even after we attached a heat absorbing glass plus a hot mirror to each of them, and used metal sheets as apertures to illuminate only the region of interest. This meant that

we had to go to higher Re than we had intended to in order to get flow induced by the particle that was much bigger and faster than the flow caused by convection. Another side-effect of the heat is that due to its strong temperature dependence, the viscosity of glycerol (see figure 3.10 (a)) continously recedes and thus the longer the experimental run takes, the bigger the Reynolds numbers Re get. This heat up is also very annoying since cooling the tank again afterwards is much harder and a very slow process.

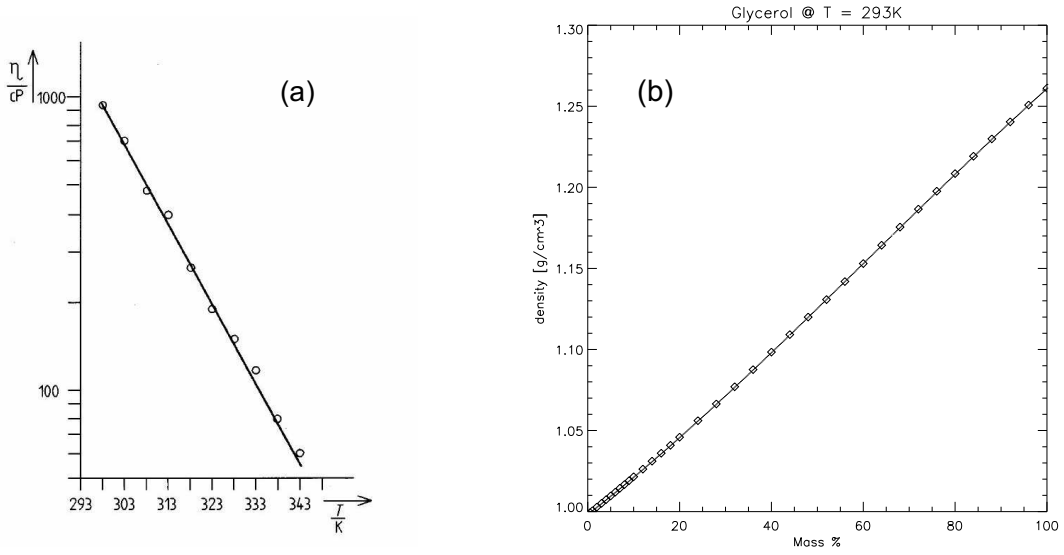

Figure 3.10: (a) Viscosity: The viscosity of glycerol has a very strong temperature dependence[8] *(b) Density: This graph is an interpolation of data from a table in [28].*

(iii) **Buoyancy** - The paramter range we had planned to explore (approx. $5 < Re < 100$ and $0 < \varepsilon < 2$) forced us to go to pretty high glycerol concentrations (a typical mixture contained about 92 % glycerol and 8 % water). Adding more and more glycerol to the mixture of course goes along with an increase of the density as well as of the index of refraction. This rather small change had dramatic effects: we originally had nice polystyrene spheres of 55 and 134 μm as tracer particles, density matched with the fluid ($\rho_{spheres} \approx 1.05 g/cm^3$ corresponding to roughly 20 % glycerol in the mixture) so that the tracer particles were floating. But at a glycerol concentration as high as 90 %, the two indices of refraction get so similar that the tracer particles almost became invisible for our cameras. And so we had no choice but to replace these high precision particles with something that would have an index of refraction further away from the one of our mixture. This proved to be a far more difficult task than anticipated, but we finally found new tracers: alumino-silicate microspheres, intended for use as filling material in low density composites and usually shipped by the barrel. After sieving them, the originally wide size distribution could be nicely narrowed to approx. 80-125 μm and they did indeed scatter enough light to be well observed. But since their density is only

[8] graph courtesy of PHYWE, "PHYWE series of publications · Laboratory Experiments · Physics", 37070 Göttingen, Germany

0.7-0.9 g/cm^3 in contrast to our new mixture (92 % glycerol, see figure 3.10 (b)) with 1.24 g/cm^3, we now suffered from a buoyancy problem. Given this density discrepency, the time for them to rise the 20 cm from the bottom to the top of the container is roughly 1.4 hours (assuming balanced forces or constant velocity). For working in the middle of the tank, the time for one experimental run should thus be much smaller than 0.7 hours or in terms of f, the number of frames per second taken by the cameras: $f \gg 3200/(0.7h) = 1.3s^{-1}$. The corresponding condition for Re is then $Re = (2aA2\pi f)/\nu \gg 7.4$. So this is another reason for going to higher Reynolds numbers, because otherwise our tracer particles will rise out of sight during the process of taking the data.

All three of these major problems could not be totally eliminated, but at least weakened by going to faster and bigger flows, namely higher Re and ε (the theoretical assumption of infinitesimal amplitude can hardly be realized in experiments anyway). Looking at the phase space diagram (figure 3.11), which shows the two distinct cases treated in detail by the theory (see section 2.2), this means that we could not access the shaded region for $|M|^2 \ll 1$ on the left. The main reason for this is that the only way to compensate for higher frequencies in order to get to low Re is a higher viscosity (both the amplitude (A) and the sphere itself (a) have to have a certain size), but the higher the glycerol concentration is, the harder it gets to maintain it: pure glycerol is highly hydrophilic and thus concentration and viscosity automatically decrease over time. So again, we are stuck at slightly higher Re than we had hoped to be able to explore.

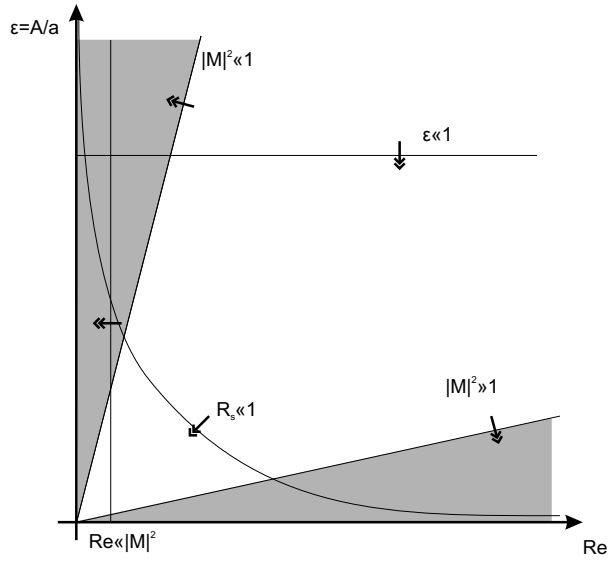

Figure 3.11: Phase-space spanned by our experimental control parameters Re and ε; lines where their theoretical counterparts $|M|^2$ and R_s are constant and the regions where they are either small or big compared to 1 are shown as well.

As a result of these constraints we focused our measurements on a Reynolds number range somewhat higher than those studied in [3].

3.4 Calibration

Another crucial part of the experiment is a proper calibration of the cameras. This means that in order to calculate real-space positions of particles as described in chapter 3.1.1, one has to know exactly where the cameras are located and where they are looking at: in other words, the parameters camera vector $\vec{c}$, viewing vector $\vec{v}$, rotation angle α and the magnification μ, so 8 parameters altogether. The problem is that these quantities are hard to measure by hand: The optical rays are passing through the water/glycerol-mixture, the plexiglas, air and the SLR-lenses of the cameras. All of this is hard or even impossible to take apart and measure directly or take into account. So we chose a direct way of using the cameras themselves for the calibration. A calibration block with a regular dot-array as shown in figure 3.12 was put in the tank filled with the same liquid as for the experiment to set up an arbitrary coordinate system.

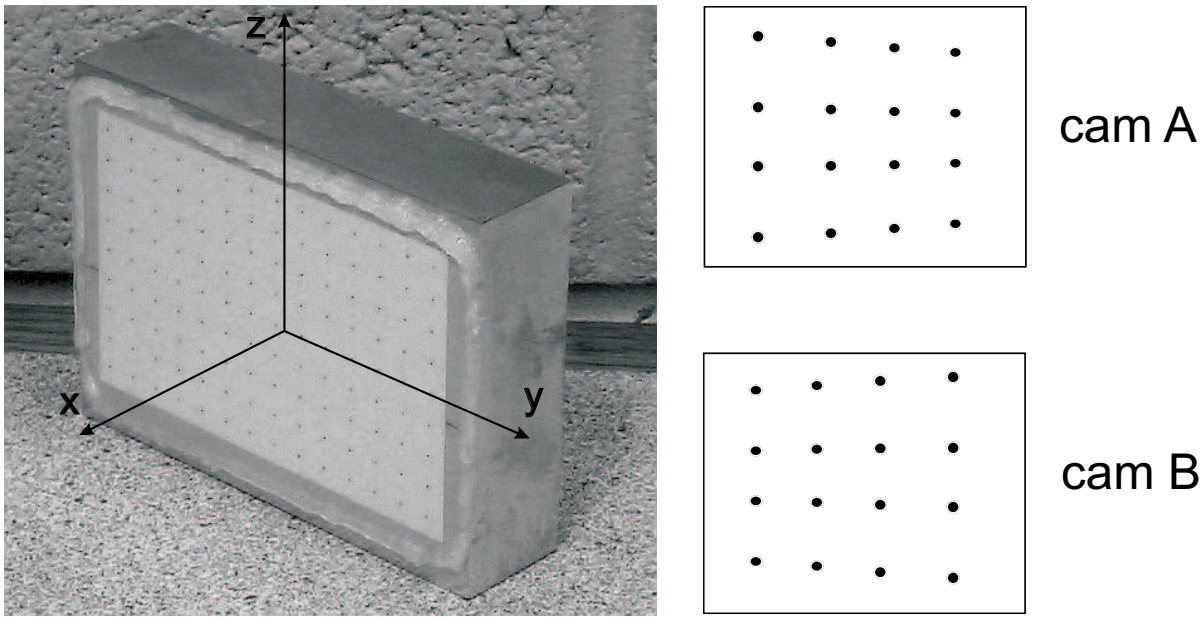

Figure 3.12: Calibration-block (photo on the left): A regular, 2-dimensional dot-array glued to one of the flattened sides of an aluminum cuboid sets up an arbitrary coordinate system in real-space, which gets slightly distorted due to perspective for the two cameras, looking at it at $45°$ *and* $-45°$ *respectively (schematic drawings on right-hand side).*

The dots are sitting on the y-z-plane, which has been flattened to within $3\mu m$. The dots have been printed on regular white paper with a 600 dpi laser printer, laminated to be water-proof and glued on the aluminum block with double-sided tape. The two cameras are looking at the block at roughly $\pm 45°$, thus leading to an image that is slightly distorted by perspective. This small distortion contains enough information to use the 2-dimensional dot-array for determining all parameters. By taking still 'calibration-images' of the calibration block, two sets of information are gained: the real-space position of the dots on the block (since they define their own coordinate system; the equidistant spaces between two dots are measured with a caliper) and their corresponding coordinates

within the images. In figure 3.13, the vectors are redrawn for further illustration of the method.

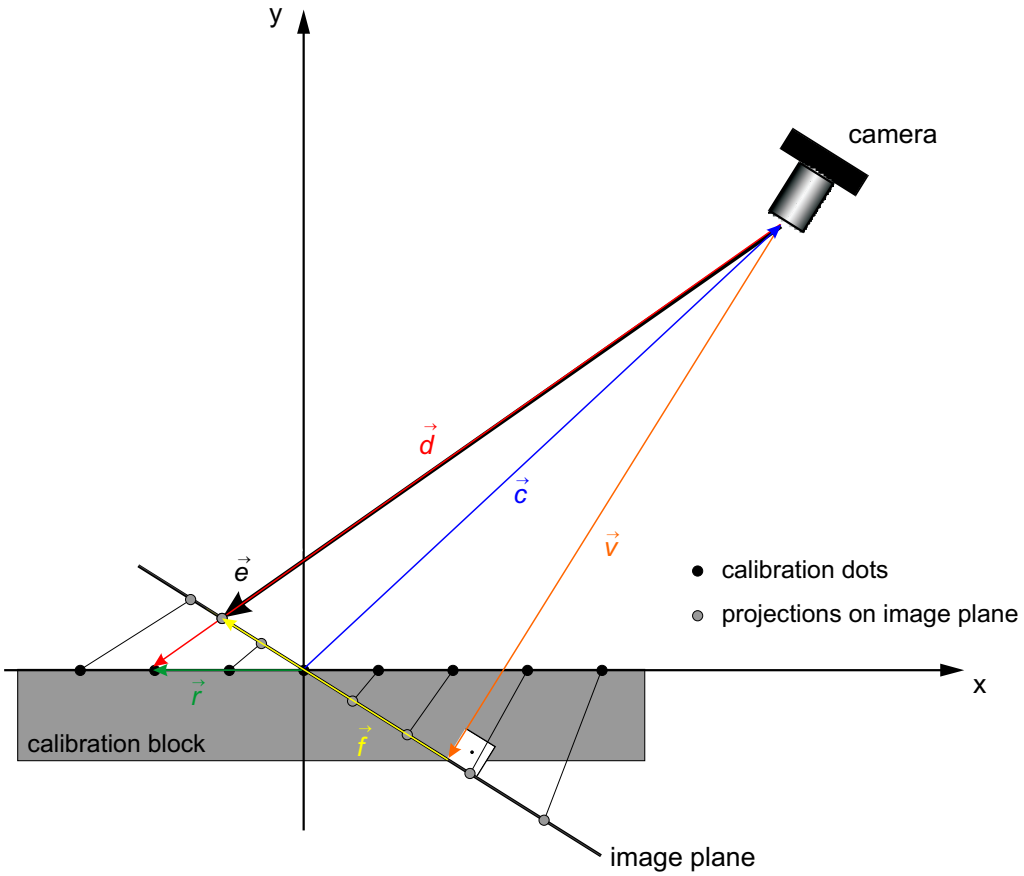

Figure 3.13: Calibration vectors: In order to calibrate, i.e. determine the position of the cameras in real-space, a calibration array of 14x9 dots was used, which defines the real-space coordinate system. A non-linear fitting code then tried to minimize the difference between 2 representations of the vector $\vec{e}$, given by the camera coordinates within the image plane and the (in this case) known position of the dots in real-space.

We thus have two distinct ways to generate the vector $\vec{e}$ (see figure 3.13): one is to use the real-space vectors $\vec{r}$, leading to

$$\vec{e}_r := \lambda(-\vec{c} + \vec{r}) \ , \tag{3.22}$$

the other to use the image coordinates, resulting in

$$\vec{e}_f := \vec{v} + \vec{f} \ . \tag{3.23}$$

A fitting program will then try to determine $\vec{c}$, $\vec{v}$, α and μ, such that the difference between the two representations vanishes:

$$0 = \vec{e}_r - \vec{e}_f \ . \tag{3.24}$$

λ is just a number to stretch (or compress) the vector $-\vec{c}+\vec{r}$ such that it connects from the pinhole to the image plane and can easily be determined by the condition that the image plane shall be perpendicular to the viewing vector:

$$\begin{aligned} 0 &= \vec{v}\cdot(-\vec{v}+\vec{e}_r) \\ \Rightarrow \lambda &= \frac{v^2}{(\vec{r}-\vec{c})\cdot\vec{v}} \ . \end{aligned} \tag{3.25}$$

The vector $\vec{f}$ is given by the same rotation and coordinate-transformation of the pixel-coordinates ${f_x}'$ and ${f_y}'$ as in chapter 3.1.1. The final equations the computer tries to fulfill by adjusting the calibration parameters are

$$0 = \lambda(\vec{r}-\vec{c}) - \vec{v} - \vec{f} \ , \tag{3.26}$$

or in components

$$0 = \lambda(r_x - c_x) - v_x + \frac{v_y\mu({f_x}'cos\alpha + {f_y}'sin\alpha)}{\sqrt{{v_x}^2+{v_y}^2}} - \frac{v_z v_x\mu(-{f_x}'sin\alpha + {f_y}'cos\alpha)}{\sqrt{({v_x}^2+{v_y}^2)({v_x}^2+{v_y}^2+{v_z}^2)}}$$

$$0 = \lambda(r_y - c_y) - v_y - \frac{v_x\mu({f_x}'cos\alpha + {f_y}'sin\alpha)}{\sqrt{{v_x}^2+{v_y}^2}} - \frac{v_z v_y\mu(-{f_x}'sin\alpha + {f_y}'cos\alpha)}{\sqrt{{v_x}^2+{v_y}^2}\sqrt{{v_x}^2+{v_y}^2+{v_z}^2}}$$

$$0 = \lambda(r_z - c_z) - v_z - \mu(-{f_x}'sin\alpha + {f_y}'cos\alpha)\sqrt{\frac{{v_x}^2+{v_y}^2}{{v_x}^2+{v_y}^2+{v_z}^2}} \ ,$$

where ${f_x}'$ and ${f_y}'$ are the camera coordinates in pixels, α is the rotation angle of the camera around the viewing vector and μ the magnification.
The fitting code required a starting guess for $\vec{c}$, $\vec{v}$, α and μ. But since c_z, μ and α gave very little variations and could be determined quite accurately by manual measurements[9], only c_x and c_y were varied around the best manual guess by $\pm 5cm$ with an increment of 1 cm in each direction (the cameras being about 40 cm away from the sphere). This resulted in 11x11=121 different solutions for each fitting run[10], with standard deviations between 2 and 6 μm around mean values from 39 to 50 cm. Apart from those pretty small deviations it is also remarkable that all of those values lie on perfectly straight lines. This means that although the fitting code does not converge perfectly, the only thing the computer does is to move the cameras slightly back and forth along a line at a certain angle. So this 'minimum' (regarding the difference between the two $\vec{e}$-vectors) is just very flat along this line. But in all other directions and for the other 3 parameters,

[9] as the camera was pretty well aligned with the x-y-plane and almost unrotated and since μ could be gained by comparing pixel-distance in the images with real distance measured with calipers

[10] The reason for us varying only c_x and c_y was actually that the code we were using to fit the parameters was for some reason more stable if the origin within the 2D camera coordinate system was shifted manually such that it coincided with the real space origin, effectively making $\vec{v} := -\vec{c}$. Although this should not affect the accuracy of our model anyway, and in fact did work quite well, we still don't fully understand the reason for the fitting code being less convergent without the shift despite further investigations on that mystery.

the minimum is pretty well defined and nicely found by the fitting routine. Results of this procedure for the two calibrations used for all of the main data are shown in fig. 3.14. Each plot shows c_y vs. c_x and one cross for each single fit.

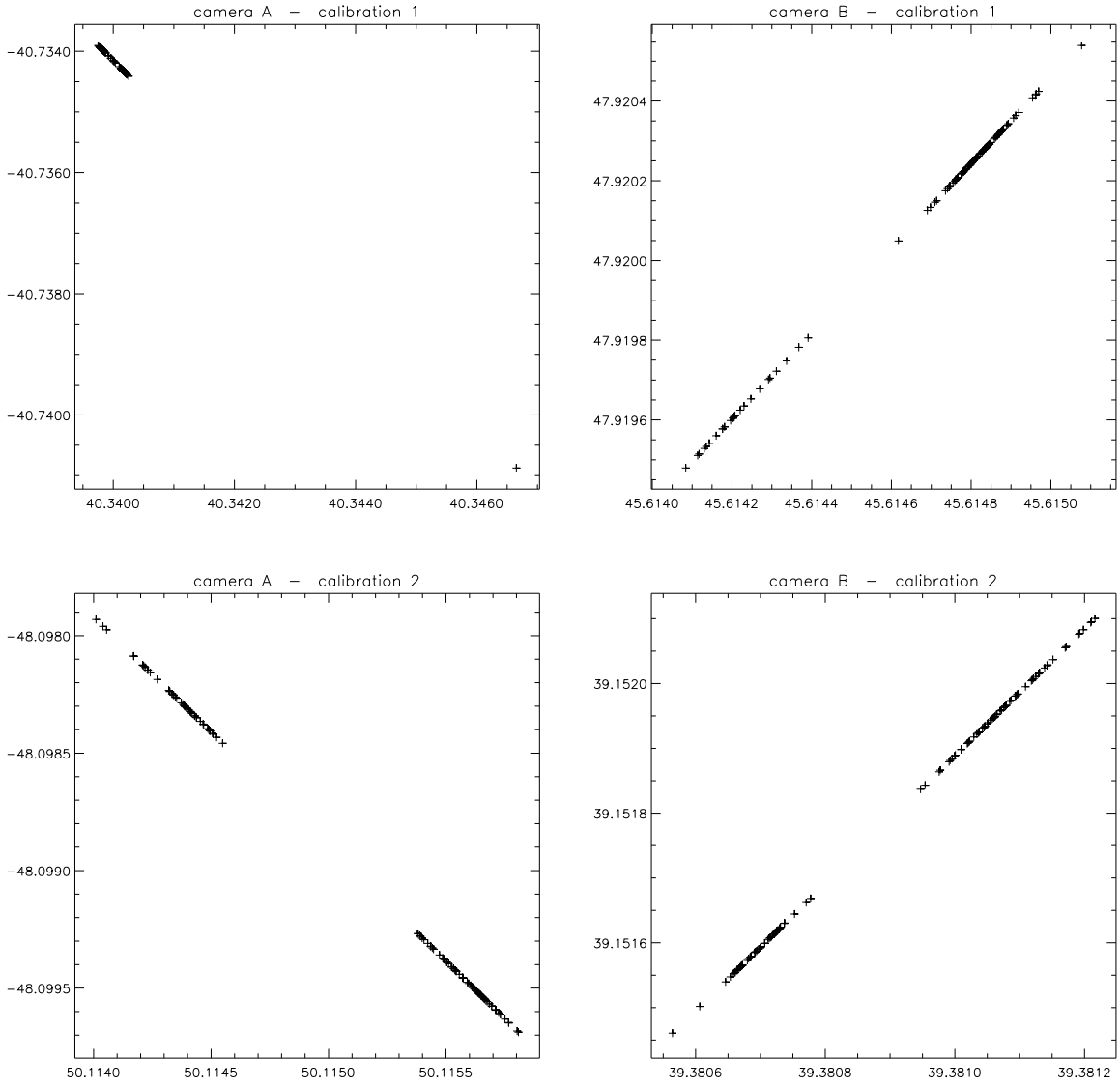

Figure 3.14: Plots of the calibration results: A fitting code produced 121 solutions for a loop of varying initial guesses and shows impressively small uncertainty in the position of the cameras (camera A sitting in negative y, positive x on the left, camera B sitting in positive x, positive y on the right; the upper two plots represent the first, the lower two the second calibration used for the main data).

3.5 Ways to analyze the video data

As described at the beginning of this chapter, the final goal of PTV experiments is to produce velocity fields, i.e. one is not only interested in the flow patterns, but also the dynamical properties of the process. Yet there is more than one way to present (and especially visualize) the results, and the main difficulties arise from the 3D-structure of the data. So in this section, I will go through different methods that can be used to present the results of such an experiment (in general and in our case). What I also want to explain here is why such experiments (still can) constitute a bit of a technical problem: the amount of data produced is enormous.

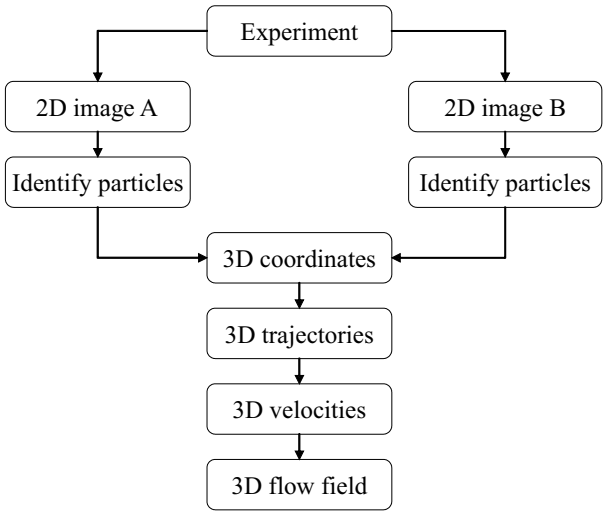

Figure 3.15: Procedure of data analysis.

First, let me remind you of the general procedure mentioned at the beginning of this chapter, shown in figure 3.15. The first step of the analysis is to extract features from the images, meaning to identify the bright spots given by the light scattering tracer-particles. For this, we used an IDL routine written by Wolfgang Losert and Greg Voth, which, after filtering the video image with a bandpass, mainly detects local maxima of brightness that are written to a results-file with their 2D coordinates (plus eccentricity, radius and integral brightness) depending on certain additional thresholds. With the 2D coordinates we then performed the procedure described by the mathematical model in section 3.1.1. The next step is to take the output of that matching program, now consisting of 3D coordinates along with the frame number (=time information), and run a 'tracking' routine (written by John C. Crocker and Eric Weeks[11]), that generates the trajectories, following the particles through space. The trajectories also contain the desired velocity information in the classical way: $\vec{v} = \Delta\vec{x}/\Delta t$. The last question, namely how to get velocity fields out of single orbits with velocities, requires some more thinking, and I will now explain three common ways to do that.

[11] http://www.physics.emory.edu/∼weeks/idl/

(i) **Full 3D phase-averaged velocity fields**

It was already mentioned above that if one seeks to get a stationary flow field, the frame of reference should be one in which the sphere doesn't move and that one way to get there is to divide the motion up into several phases. Since we have a total of 16 equidistant holes around the edges of the disk, we can choose any factor of that number: the full 16, 8, 4, 2 (or 1) phases. One then analyzes each subset of images belonging to one phase separately and gets a stationary flow field for that specific position (and direction) of the sphere. The amount of data produced during one sequence in this case is, at for example the full 16 phases and 5 Hz motor frequency, $16 \times 5Hz = 80fps \rightarrow 80MB/s$. This is already a little faster than the current harddisks are able to write data. But since the cameras are connected to their frame grabber cards by two fast serial cables, this is not a problem. Yet another one does occur: In order to get 3D velocities, one takes all particle tracks, calculates the appropriate velocities and then splits up the space into small bins by means of a certain grid size. The average velocity in each bin then defines the velocity at that region in real space. But for those boxes and average velocities to make sense, one has to have a certain minimum density of registered particles with velocities in the observed volume. If, for example, there are approximately 50 particles in each frame (meaning 50 particles that have been matched successfully and that gave velocities), and we still work with the 16 different phases like before, we have a total of $(3200 \cdot 50)/16 = 10000$ particles per phase in each sequence (1 sequence $\hat{=}$ 3200 images). So, if we divide the 1024 x 1280 pixels up into 64 x 80 bins (one bin would then be 16 x 16 pixels), which means in 3D 16 x 16 x 16 pixels, the number of bins would be $64 \cdot 80 \cdot 80 = 4.096 \cdot 10^5$. A reasonable minimum number of particles per bin (for this kind of statistical averaging) would be for example 5 (this is a completely arbitrary example, just to give some numbers). This means

$$5 = \frac{\text{total \# of particles}}{\text{total \# of bins}} = \frac{(\text{\# of seqs}) \cdot (\text{\# of particles per seq})}{\text{total \# of bins}}$$

or that we need to take

$$\frac{(\text{density}) \cdot (\text{total \# of bins})}{\text{\# of particles per seq}} = \frac{5 \cdot 4.096 \cdot 10^5}{10000} = \text{\# of seqs} = 204.8$$

sequences in order to arrive at the desired average density of 5 particles per bin. Yet since each sequence is approximately 4 GB, the size of our hard disks (600 GB) would already be too small: $204.8 \cdot 4$ GB = 819.2 GB. So with only one set of parameters we would already have to take more data than we can store. This is a significant problem. It can be surmounted by an increase of the bin-size (which decreases the spatial resolution), a higher particle-density per image (which is hard to achieve with only two cameras in use as described above), less phases (meaning more particles per phase and thus less sequences in order to get the same density) or zooming in (which would allow to deal with a higher particle density in real-space, or no loss of spatial resolution with bigger bins).

Assuming these problems can be solved, this first method gives full 3D velocity fields for a given number of phases.

(ii) **2D azimuthally-averaged velocity fields**

Another way to look at the results is to make use of the cylindrical symmetry inherent in the process: the sphere is moving only vertically along the z-axis, and thus all particles at the same height and the same distance away from the axis of oscillation should behave the same way. This is a very practical approach, because it is then possible to visualize the flow field in 2D: a color-coded z-r-plot, where color indicates the velocity, tells the whole story (at least for one component of the velocity). Also, the amount of data needed for reasonable statistics is two orders of magnitude smaller than in the former example: for simplicity, let us assume a constant bin size in 2D (z-r), even if then the bin size in 3D increases with increasing r (distance away from the axis of oscillation), since the annulus over which we will average gets bigger and bigger the further away from the center we are. So, with a bin size of 32 x 16 pixels[12], which gives 40 x 64 = 2560 bins and the total number of particles per sequence again 7500 (if we still use 16 phases), we would thus need (5 x 2560) / 7500 = 1.7 sequences for the desired minimum density. This means we can even increase our demands regarding the average density or spatial resolution by taking a few sequences more than that.

(iii) **Periodic Displacement**

The third method is to just take a look at the periodic displacement of the particles, which in some sense corresponds to the long-term or average motion. In this case, only one of the 18 holes in the disk is opened, and the process of taking the data consumes much more time. Regarding the practical side, we would now have only one phase, and thus the full 50 x 3200 = $1.6 \cdot 10^5$ particles per sequence. At the same bin size as in the first example (16 x 16 x 16 pixels), there would be again $4.096 \cdot 10^5$ bins, and so (5 x $4.096 \cdot 10^5$) / $1.6 \cdot 10^5$ = 12.8 sequences would be necessary.

Of course, the methods can (and will) also be combined: for example, it is hard to illustrate full 3D fields on a 2D sheet of paper, so the azimuthal average provides a very good last step in order to simplify the results in both the periodic displacement and the phase-average case.

Unfortunately, the technical side restricted our ability to perform this last step (velocity fields): our 600 GB hard-disks were just not enough to store all the data that would have been necessary for decent statistics. Besides, since 1 sequence is already 4 GB of data, even our DVD-burners could not solve that problem (burning hundreds of DVDs is not a very practical solution and very time consuming as well). Pre-processing the images while capturing would dramatically reduce the amount of data: a sequence would then be a few MB instead of GB! But since the appropriate hardware is not yet available, we were stuck with our problem of dealing with almost 1 Terabyte of raw data (.tif-images) altogether for this thesis. Apart from that, our experiment would easily allow for getting the velocity fields.

[12] 32 instead of 16 as above, because in a z-r-plot, it doesn't matter on which 'side' of the sphere you are

Chapter 4

The results

Since the main reason for building this experiment was the interesting behavior of particles in a vibrated fluid (see [3] and next subsection), which was explained by the flow field created around a single sphere oscillating in a viscous fluid, we first explored the case of a single sphere, starting with taking data in the middle of the tank, where no boundaries should affect the flow. This already revealed some interesting discrepancies with the theory. We then went on and studied the changes that result from the presence of the bottom plate. A very dramatic change of the flow geometry even around a single sphere could be observed there. The last set of experiments was conducted with a pair of spheres, sitting a fixed distance apart, both in the middle and directly at the bottom of the tank. This also showed that the original explanations for the attraction and repulsion of shaken particles as seen in [3] are a bit too simple for what is actually going on.

4.1 Flow field around a single sphere

4.1.1 General aspects of undisturbed motion in the middle of the tank

First, I want to show what the main features of such an ideal flow-field around an unperturbed single sphere should be (in a typical parameter regime). Figure 4.1 is taken from *"An album of fluid motion"* [6] and shows the flow field around a cylinder: one looks along the axis of the cylinder, which performs up and down oscillations of small amplitude at fairly high Re (A/a=0.17, Re=140). Here and throughout this chapter, the Reynolds number is based upon the diameter of the sphere,

$$Re = \frac{2aA\omega}{\nu} \quad , \tag{4.1}$$

in order to make it easier to compare the numbers to the ones in [3]. A simple way of describing the flow is that the cylinder irreversibly pushes fluid away above and below itself during the oscillations, and because of the incompressibility some liquid has to compensate for this by flowing toward the cylinder in the center plane perpendicular to the stroke. Next to the cylinder there are inner recirculation zones, with an opposite rotational direction. Although this is basically a 2-dim. flow, it can be 'extrapolated' to the 3-dim. case in a rather general way. The size of the different zones and their exact shape do not have to match the ones seen in this example, but it is to be expected that

the flow around an oscillating sphere should look pretty much the same, if 'cut' and plotted on a plane that contains the axis of oscillation. An example of one of our most regular flows in the middle of the tank is shown in figure 4.2. Unless otherwise stated, these kinds of plots always show periodic displacements (i.e. sequences of one image per cycle, usually taken at the center of the stroke), and the cylindrical symmetry of the problem (a single sphere oscillating along the z-axis) allows us to collect all data at a fixed distance away from the center of the sphere (all different azimuthal angles φ) and plot only z vs. r, i.e. height vs. distance from the center. Plots of v_φ and x-y cuts respectively confirm that the motion is almost entirely radial in our experiments, although there are of course some minor deviations (one of the sources for crossing tracks in the z-r-plots). The radial velocity component v_r , given by the color map as the third dimension, ranges from roughly -0.446 cm/s (blue) to 0.417 cm/s (red). The position of the sphere at the center of the stroke is indicated by the semicircle.

There is a slight up-down asymmetry and we had some problems to reveal the inner structure next to the sphere, but the overall flow geometry is resolved well. There are some mismatched particles resulting in 'wrong' tracks (the ones that cross the direction of the majority and the ones 'inside' the sphere), which I will talk about later in this chapter. As already stated above, the setup restricted our access to certain regions in phase space, such that reproducing the exact match to the Haverford data ([3]) was not possible. However, we were still able to resolve a good portion of interesting features of the flow at slightly higher Re-numbers. The problem was that, although the rod we used to attach the sphere to the driving mechanism was only about 1/12 the diameter of the sphere, we still saw significant distortions of the flow geometry due to its presence (as already discussed as one of our major problems in section 3.3.2). Figure 4.3 shows sequences of runs taken at fixed A/a at increasing Re. At low Re, the rod significantly distortes the picture: the sphere sits at the origin, and one can clearly see that the upper recirculation zone is pushed down beneath the equator, as is the inflow outside this inner region, which, according to the symmetry of the sphere, should be perfectly horizontal at the equator. This effect gets less and less important as the Reynolds number is increased, and above $Re \approx 20$, the flow is almost symmetric, in a sense that then at least the inflow is horizontal. At higher A/a (i.e. at higher amplitude), the influence of the rod on the geometry becomes also less important. At medium Reynolds numbers ($15 < Re < 25$, also depending on the amplitude), there is still a slight up-down asymmetry, but since the most interesting thing for us is the general geometrical features and the inflow velocities at the equator, we can neglect those side-effects, as long as we work at high enough Re.

Before I go into the details of our flows, I have to describe what happened in the experiments conducted at Haverford (→ [3]) to be able to compare the results: a cylindrical aluminum container was put on an electromagnetic shaker and a submonolayer of small steel spheres ($a = 0.397mm$) in a water/glycerol mixture was filmed from above (see figure 4.4); illumination from an oblique angle then also allowed the determination of their vertical positions. The Reynolds number Re, based upon the diameter of the spheres, ranged from 2 to 10.

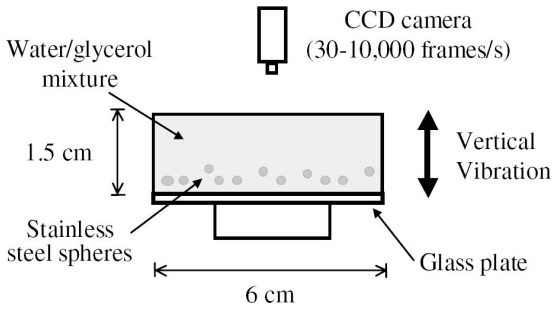

Figure 4.4: Setup of the Haverford experiments (taken from [3]).

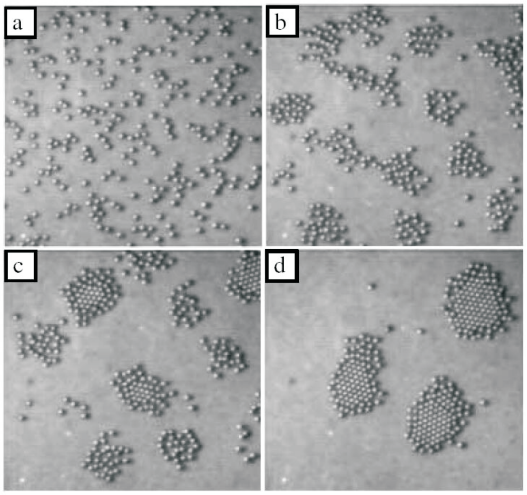

Figure 4.5: Time evolution: An initially random distribution of beads is collected into clusters very quickly by the attraction created by the streaming flow ($Re \approx 5$): (a) $t = 0s$, (b) $t = 8s$, (c) $t = 16s$, (d) $t = 32s$ (taken from [3]).

Figure 4.5 demonstrates how an initially random distribution of particles quickly gathers into clusters. This attraction could be shown to have its origin in the interaction with the surrounding fluid rather than in the inelastic nature of the collisions. Very good agreement with the steady streaming prediction could be attained, shown in figure 4.6. A direct explanation comes from the steady streaming around a single particle (see figures 4.1 and 4.2): the pumping of fluid towards the sphere in the equatorial plane should create such an attraction. A more interesting thing happened at larger amplitudes of the shaker[1] and thus higher Re: the distance between two spheres suddenly jumped from contact to a nonzero separation, whereas the amplitude A of the particles bouncing of the bottom plate showed no such transition. This is displayed in figure 4.7. The onset of repulsion was thought to originate either from the inner recirculation zones or a change in the importance of the oscillatory boundary layer as oppose to the steady one, but could not be explained satisfactorily at that time, and was one of reasons to build my experiment. Further investigations in [3] showed a variety of patterns, including regular, stable structures as well as dynamic and chaotic ones [2].

[1] the control parameter used for this experiment was defined as $\Gamma := (\omega^2 S)/g$, where S is the amplitude of the shaker, ω the frequency and $g = 9.81m/s^2$ the acceleration of gravity

[2] see http://www.haverford.edu/physics-astro/gollub/clustering/ for animated movies and details

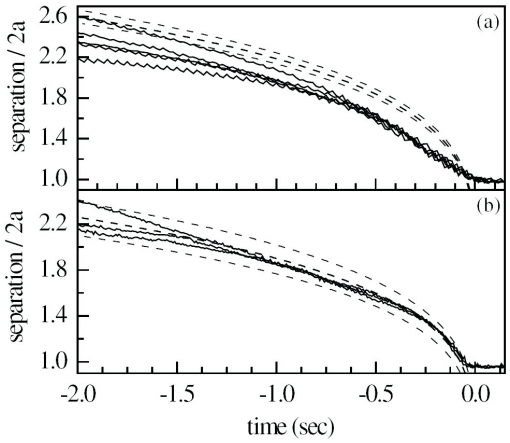

Figure 4.6: Approach of two spheres over time as measured in the tank (solid lines) compared to the theoretical steady streaming prediction (central dashed line with uncertainty of measuring the amplitude in the experiment). Shown are two experimental runs with different frequency and amplitude, but roughly the same Re (≈ 5; taken from [3]).

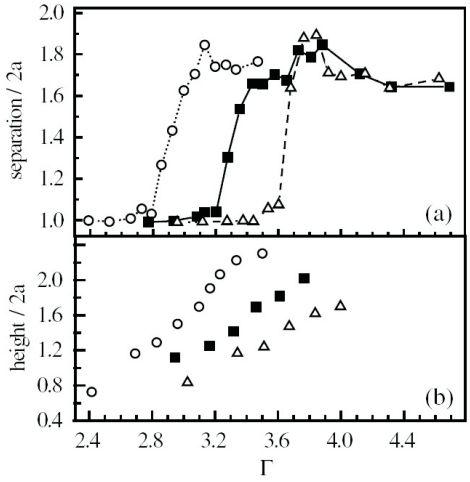

Figure 4.7: Sudden repulsion: While the equilibrium distance between two particles suddenly jumps from contact to a nonzero separation (a), the peak to peak height $2A$ that the particles bounce of the bottom plate shows no dramatic change (b). The three curves belong to 17, 20 and 23 Hz respectively (left to right), and $4 < Re < 10$ (taken from [3]).

These are the main results from [3], and since those experiments built the basis for mine, I will compare the outcome of both regarding the following points: (i) size of the recirculation zones (source of repulsion) as indicated by the equatorial stagnation point r_s both as a function of Re and $A/a = \varepsilon$, and (ii) inflow velocities ($v_r(\theta = 90°)$) again as a function of both, Re and $A/a = \varepsilon$, since there have been two dramatically different theoretical predictions for them. We find that regarding (i), the position of r_s moves in with increasing Re and is way too far out at low Re to even account for the attractive part.

The dependance of the position of this stagnation point on the amplitude ($A/a = \varepsilon$) on the other hand will be shown to be non-monotonic in disagreement with the simple idea of a viscous penetration length, which monotonically increases with A/a. Interestingly enough, the maximum extent of r_s occurs right in an amplitude range where the sudden onset of repulsion was observed in [3]. The comparison between the two theories on the one hand (Brenner/Stone as in [3] and Riley [14]) and my experimental data on the other hand reveals that not only do the two theories differ dramatically from each other, but also from my results. Apart from the absolute values, which are off by a factor of 1/3 and 50 respectively, even general trends are predicted wrong. The last step in this section will be a comparison between the two theories and a recent simulation (see [23]), and again, all three disagree fundamentally.

In detail, my results are the following: one feature of the flow around a single sphere, which can be seen very nicely in figure 4.2, is the stagnation point at $\theta = 90°$, i.e. in the equatorial plane, called r_s here. It is the point where the upper and lower inner doughnut-shaped recirculation zones collide with the outer inflow, which itself gets separated into upper and lower half. The reason for this point being important is that it marks the border of the repulsive part of the steady streaming: the radial velocity at the equator changes its sign from going outward to pumping towards the sphere. This point shows some interesting behavior in our experiments: (i) The position of r_s as a function of the Reynolds number Re is shown in figure 4.8. It contains several runs with different amplitudes; two runs were performed with a bigger sphere (diameter of 5 cm instead of the 2 cm we usually used) in order to get to the higher Reynolds numbers. One can see that r_s moves closer to the sphere as Re is increased. This alone is probably not very surprising, since even the simple idea of a viscous penetration length (or oscillatory boundary layer thickness)

$$L_\nu = \frac{\sqrt{\nu/\omega}}{2a} = \frac{\sqrt{\frac{2a^2 A/a}{Re}}}{2a} = \sqrt{\frac{\varepsilon}{2Re}} \tag{4.2}$$

(normalized by the particle diameter $2a$) tells us that it should really move further in (although the magnitude of this scaling length is too small roughly by a factor of 10), which is also shown in the plot. For simplicity, only the theoretical values of L_ν for the lowest (0.3) and highest (2.0) ε are shown in the plot, all the others lie in between the two.
More interesting is the fact that (ii) at lower Re, the actual position of the stagnation point is way too far out for this single-sphere flow geometry and the inner recirculation zones to account for both the attraction until contact as well as the repulsion seen in [3]. Comparing the actual distances in figure 4.7 and 4.8, the two spheres in [3] jump from contact to less than 2 particle diameters (where they stabilize again) at $4 < Re < 10$, whereas in my experiments, the position of the stagnation point and thus the border of the recirculation zones shows a trend towards much bigger distances for Re less than 20. This trend is confirmed by the theory (see figure 2.1), which tells us that for very small Re, the recirculation zones become bigger and bigger until they dominate the whole steady streaming[3], resulting in 'inverse' pumping, i.e. from the poles towards the equator. This is a first hint at two-particle-effects being responsible for the repulsion, the flow field

[3]although no statements about the transition between those regimes have been made

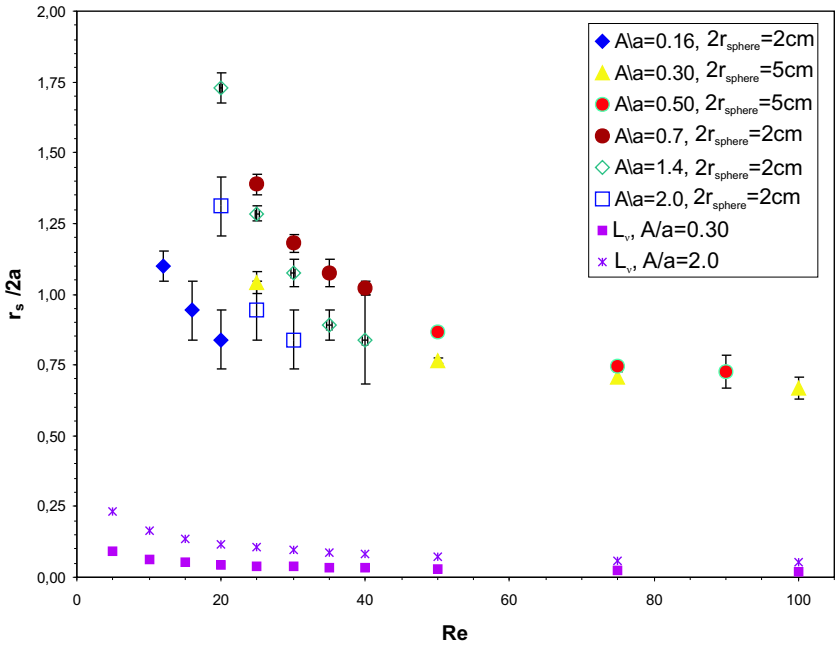

Figure 4.8: Position of the stagnation point r_s as a function of Re at different A/a.

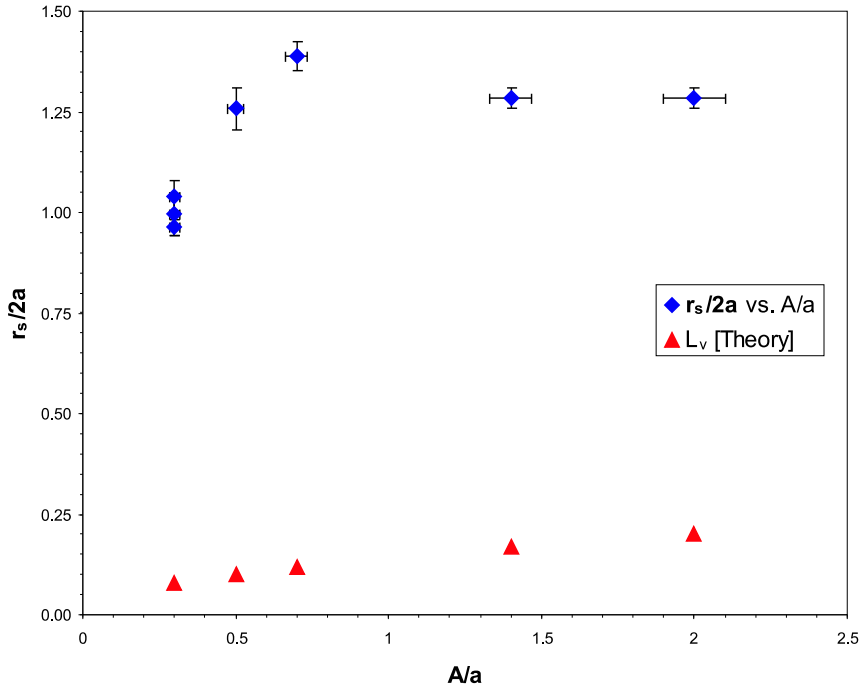

Figure 4.9: Position of the stagnation point r_s as a function of A/a at fixed $Re = 25$.

around a single sphere as observed in my experiments cannot account for that. But it also shows that even the attractive part of the interactions in [3] is not fully understood, since the region where attraction would be expected is inside the stagnation point. (iii) Another interesting behavior is revealed in figure 4.9, which shows the position of r_s as a function of $A/a = \varepsilon$. The size of the recirculation zones obviously has a maximum at a certain amplitude, quite in contrast to the monotonic increase predicted by L_ν. While our experiments were performed at much higher Re, the amplitude of this maximum lies right in the range where the sudden repulsion was seen in the Haverford experiments (compare to figure 4.7). Although the flow field around a single sphere does not provide a sufficient explanation for those phenomena, there seems to be a relation between this maximum and the repulsion.
The next thing I want to take a look at are the inflow velocities at the equator, since I have two fundamentally different theoretical predictions for those (see end of theory section, 2.2.3). This feature of the flow can be nicely extracted from our data by taking

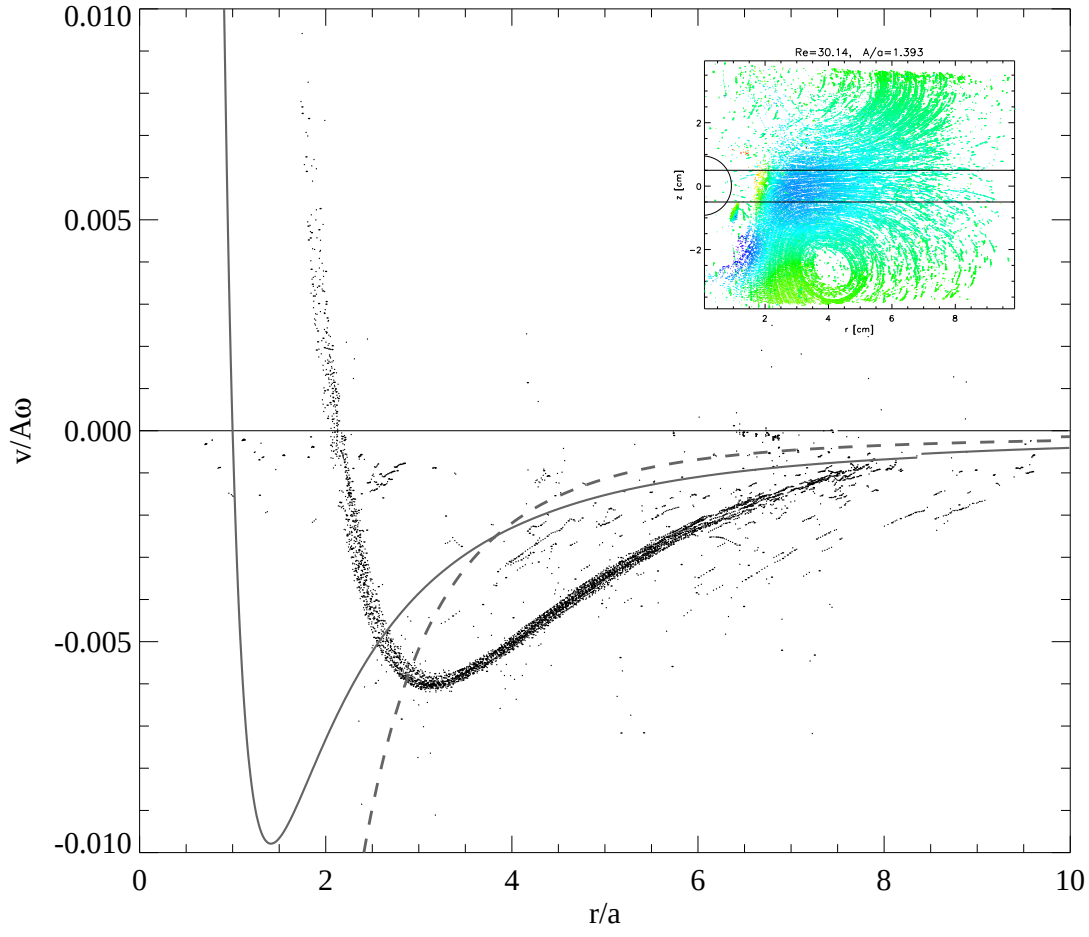

*Figure 4.10: Cross-section of steady inflow velocity v_r vs. r in a small stripe around $z = 0$. The scattered points are experimental data ($Re = 30$, $\varepsilon = 1.4$, $R_s = 42$, $|M|^2 = 21.4$), compared to the theoretical calculations of Riley (solid line, IMPORTANT:***divided by 50!!***) and Brenner/Stone (dashed line).*

a small stripe around $z = 0$, e.g. $-0.5 < z < 0.5$ and plot the radial velocities of all particles inside this band versus the radial distance r. According to their calculations, Riley [14] predicts

$$u_r(r, \theta = 90°) = -\frac{45}{32}\frac{\varepsilon}{r^2}\left(1 - \frac{1}{r^2}\right) \ , \tag{4.3}$$

whereas Brenner/Stone [3] conclude

$$u_r(r, \theta = 90°) = -0.53A\sqrt{\omega\nu}a^2\frac{1}{r^3} \ . \tag{4.4}$$

An important point to notice is that these calculations were done for certain limits (both assume $\varepsilon = A/a \ll 1$ throughout and $|M|^2 \gg 1$; but then Riley works with $R_s \ll 1$, whereas Brenner/Stone have $R_s \gg 1$, assuming a potential flow in the outer region) and only for the far-field steady inflow velocity (at $\theta = 90°$).

The plot in figure 4.10 reveals the strong discrepancy between the theories and my experiment. The values from Riley's theory (solid line) have been divided by 50 (arbitrary number!), to fit the whole graph on the same plot with my data (scattered points) and the Brenner/Stone theory (dashed line). Both predictions are far off the real data, presumably mainly because of the impossibility of realizing an infinitesimal amplitude in a real experiment. On the other hand, we think that there is also a chance of viscous effects becoming important in the R_s-regime (10-50) that we study, which were neglected in the Brenner/Stone-calculations. Again, the lack of a maximum and a stagnation point respectively in the Brenner/Stone plot are to be expected as well as the constant positions (no dependance on Re or ε) of the maximum and the stagnation point in the Riley plot. Because of these problems with the theories, it is rather hard to compare further details between experiment and theories, but one more thing to do is looking at the velocity dependance on Re, shown in figure 4.11. Instead of taking the maximum of v_r, certain points had to be picked: v_r at 2d (= twice the sphere diameter away from the center of the sphere), 3d and 4d. What is most concerning about this plot is the fact that the theory (Brenner/Stone) even gives a wrong trend: decrease of v_r with increasing Re, whereas the experiments show the opposite.

The dependance of v_r on the amplitude A/a is shown in figure 4.12: the inflow velocity thus increases monotonically (but not linearly as predicted by equation 4.4) with increasing amplitude (at least as far as our measurements go; it will presumably drop down at higher Re again).

All in all, the theories do not seem to be able to accurately describe what is going on in the regime accessible in our experiment. The possible reasons for this in our view are the non-infinitesimal amplitude and viscous effects, which seem to become more important in the range of $10 < R_s < 50$. A big problem there also is that it is just not at all clear what $R_s \ll 1$, $|M|^2 \gg 1$ or $Re > 1$ means explicitly.

There has also been a recent (2002) numerical simulation by H.M. Blackburn [23] on "Mass and momentum transport from a sphere in steady and oscillatory flows". In his paper, he reproduces the profiles of cycle-average radial velocities over the full range ($0 < r < 10 \cdot r_{sphere}$, and apparently his results would be in good agreement with real flows apart from the fact that he also concentrates on limits that are inaccessible in our experiment ($\varepsilon = 0.1$ and $\varepsilon = 5$). So again, I can't really compare his results with mine, however, figure 4.13 does the comparison between the theories and his simulations. And again, these also do not agree very well. Our final conclusion so far is that the two

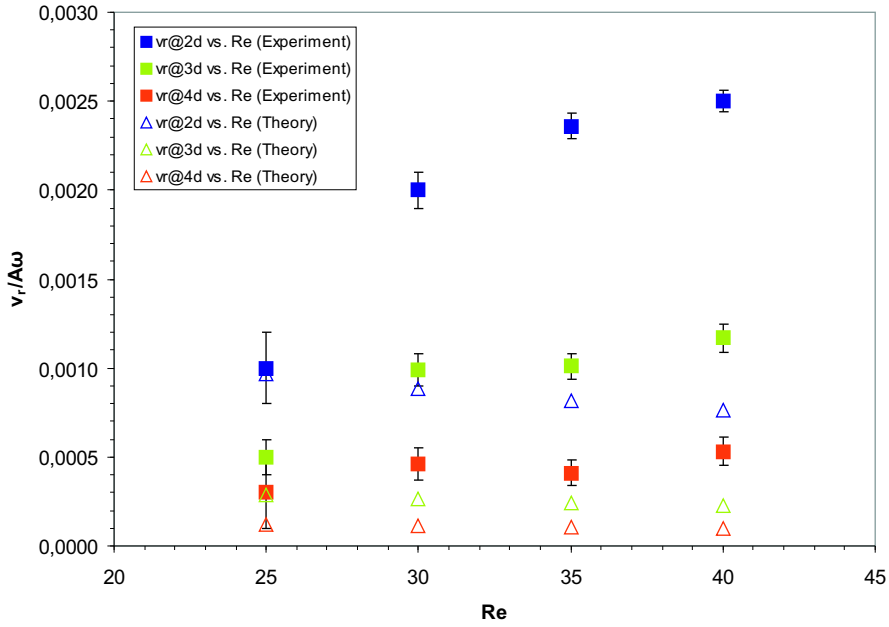

Figure 4.11: Steady inflow velocity v_r as a function of Re at fixed $\varepsilon = 0.7$, comparison between Experiment (filled squares) and Brenner/Stone-theory (open triangles).

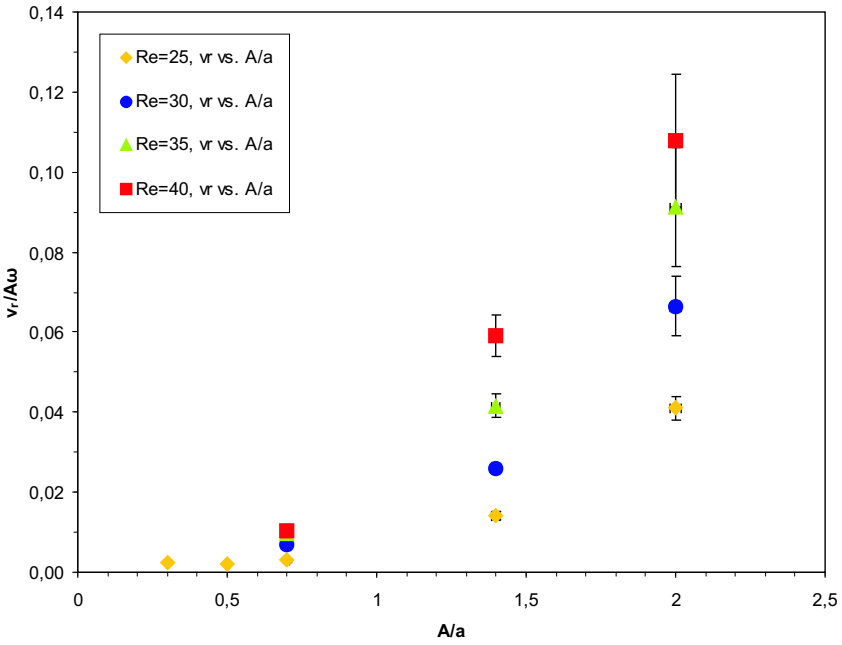

Figure 4.12: Steady inflow velocity v_r as a function of $A/a = \varepsilon$ at fixed Re.

theories represent two different limits and are likely to be consistently correct in these, but that our experiment lives somewhere in between. It remains as a challenge for future work of both experimentalists and theorists to try to investigate in the regimes of common parameters, especially since many applications of streaming flows are in the large amplitude and moderate R_s range.

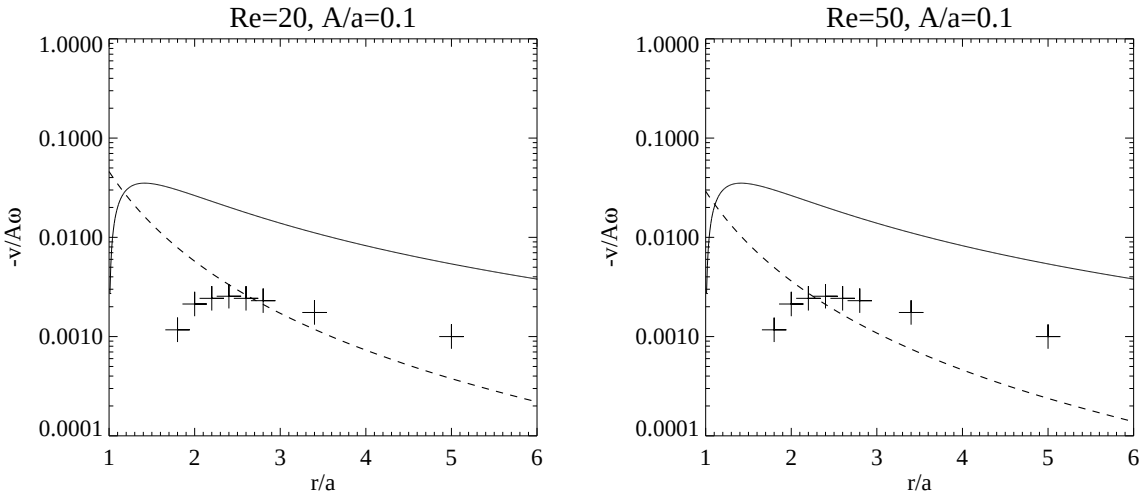

Figure 4.13: (Modulus of the) Steady inflow velocity v_r along the equator ($\theta = 90°$) as a function of distance away from the center of the sphere. Solid line is the theory by Riley (1966), dashed line is the theory by Brenner/Stone (2002) and cross symbols are numerical simulations by Blackburn (2002).

4.1.2 Changes of the flow field due to the bottom plate

The next set of experiments dealt with bringing the sphere closer to the bottom plate of the tank, which corresponds to the situation in [3], where the spheres bounced off the bottom of the electromagnetically shaken container (see figure 4.4).

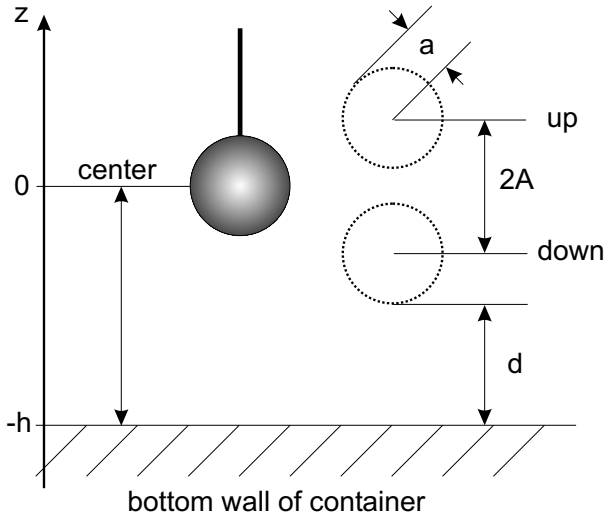

Figure 4.14: Definition of 'distance to the bottom plate': the distance d refers to the space between the lowermost point of the sphere during the stroke and the bottom plate (and is normalized by the particle diameter). The following data plots will have the center of the sphere at $z = 0$ throughout, with the images taken at the center of the stroke.

We thus took 5 single sequences at different distances to the bottom plate (see figure 4.14 for clarification) at fixed Reynolds number and amplitude ($Re = 30$, $\varepsilon = 0.7$), and saw a rather dramatic change to the flow geometry: not only does it get distorted by the presence of the boundary, but finally totally changes its topology! As can be seen in the 5 data plots of figure 4.15, the lower outer inflow region successively closes in, gets compressed and eventually joins the upper inner recirculating 'doughnut'. This quite different topology results in a much bigger repulsive region than the simple idea of explaining the phenomena in [3] would allow. In addition, in the parameter regime of lower Re, where the Haverford experiments [3] were done, this repulsive region is most likely to become even bigger. This clearly indicates that one has to think about 2 particle effects in order to come up to the attraction and repulsion of 2 (or several) particles. In [3], it was assumed that the far field inflow velocities of two spheres can be added linearly to get the rate of approach given that (i) the oscillatory boundary layer is small compared to the steady boundary layer, (ii) the particles are far enough apart that they do not affect each other's boundary layers, and (iii) the influence of the bottom plate can be neglected. These assumptions were thought to hold (i) when the driving amplitude was

Chapter 5

Conclusion

Since there were two distinct purposes of this thesis, namely an experimental (implementation of the PTV system) and a physical (exploration of the flow field around an oscillating sphere) one, I also want to draw two parts of conclusions.

Starting with the technical side, I can say that first of all, we achieved very good measurements of the flow fields even with our two-camera setup and both the simple mathematical model and calibration procedure despite starting from scratch and building the whole setup plus conducting the experiments in the short period of 12 months. We could sufficiently overcome the problems we encountered regarding convection in the tank due to warm-up by the theater lights by using heat-absorbing glass and hot mirrors, the disturbing effects of the rod that attached the sphere to the driving mechanism and the buoyancy of our tracer particles by going to slightly higher Reynolds numbers as well as some minor difficulties. With our calibration we could determine the position of a 100 μm particle to within 5-10 μm at a standard deviation of about 5 μm. This could easily be improved even further with a more complex calibration and the use of three or four cameras, eliminating the ambiguities arising with a two camera setup and cutting down the number of mismatches to a minimum. Besides, our setup allowed precise measurements of both the phase dependance of the flow field as well as a resolution of the full three-dimensional flow around two spheres oscillating (in phase) at a fixed distance. The main limitations to our system are non-passive tracer particles due to buoyancy and convection, and mismatched particles due to the ambiguities arising from the use of only two cameras (instead of three of four). The first constraint made us work at slightly higher Reynolds numbers and thus faster flows than we had originally intended.

The physical questions we tried to address were given by an earlier experiment conducted at Haverford ([3]), which reported complex self-organizing structures consisting of non-Brownian particles bouncing of the bottom plate of a vibrated container filled with a viscous fluid. The steady streaming around these spheres could be tuned to produce a variety of patterns through long-range attraction and short-range repulsion. By that time (2002), the attraction could be modeled and explained using the existing theory of the steady streaming around a single oscillating sphere, whereas the repulsion remained as a question yet to be resolved. This built the starting point for using the experimental setup to investigate the flow field around an oscillating sphere.
In the middle of the tank and at typical, moderate flow parameters, we could nicely reproduce the well-known flow geometry around an oscillating sphere: the main features are

an outer pumping flow from the equatorial plane towards the axis of oscillation separated from inner recirculating zones next to the sphere with an opposite rotational direction. Regarding the details of this streaming, we find that most of the assumptions previously used to explain the interactions between these particles, namely considering only the flow field around a single sphere, ignoring any boundary effects by the container walls, are not justifiable. First of all, the flow geometry experiences a dramatic change if the sphere is brought closer to the bottom wall of the container (at typical flow parameters): not only does it get distorted by the boundary, but finally has a totally different topology than in the middle of the tank. Two regions of the flow originally separated from each other by a stagnation point, where one of them effectively is repulsive, the other attractive, coalesce to result in one huge, repulsive zone extending over more than two particle diameters. This already inhibits the use of a single particle theory to even account for the attraction until contact observed in [3]. Although the experiments there were conducted in a range of parameters not accessible in our case, it is most likely that they would show an even bigger extent of this repulsive region. Our final conclusion in that regard is that clearly two-particle effects must be responsible for both, attraction and repulsion, as seen in [3]. We thus also made measurements of the full three dimensional streaming around two spheres, which support that statement.
Secondly, we could identify several discrepancies with the existing steady streaming theories, arising presumably from experiments and theories working in different parameter regimes; the necessity of using a non-infinitesimal amplitude of oscillation in experiments as well as the neglect of viscous effects in some theories lead to dramatically different results in the two cases. Even in the middle of the tank, we find that the extent of the inner recirulating zones next to the sphere, which were thought to cause the repulsion, is way too big at higher Reynolds numbers than in [3], and again will be even bigger at lower Reynolds numbers without much doubt. The dependance on amplitude of the size of these zones was shown to have a maximum in pretty much exactly the same range were a sudden onset of repulsion was observed at Haverford. This seems to be a good starting point for further investigations on this phenomenon.
While we had two different theoretical predictions for the steady inflow velocities along the equator from two different approaches, our experiments are found to align with neither of the two. Apart from being off in the magnitudes by a factor of 50 and 1/3 respectively, even a general trend is predicted wrongly: our inflow velocity increases with increasing Reynolds number, whereas the theoretical values decrease for one theory and show no dependance on the Reynolds number at all for the second one. Finally, both theories also disagree fundamentally with the results of a recent numerical simulation [23], which, although being close to experimental results, also concentrates on parameters inaccessible with our setup.

All in all, the implementation of the PTV system can be seen as a full success, providing an optimal ground for the construction of the next set of experiments in our group, which will be building a $1m^3$ turbulence tank to be observed with the high speed digital cameras as well. On the physical side, I hope to inspire further experiments and theories concentrating on two-particle effects to come up with a good explanation of the complicated interactions between several oscillating particles.

Appendix A

Experimental details

The experimental problems we encountered, some of which are described in detail in section 3.3.2, required modifications and additional features of our original design. For example, the heat generated by the 750 Watts theater lights had to be absorbed somehow in order to minimize the convection, but on the other hand, we couldn't afford to lose too much visible light. So we first tried to use heat absorbing glass, a quite cheap solution with the disadvantage of also taking out a considerable amount of visible light. Apart from that, they didn't remove enough heat and additionally get pretty hot. So we decided to spend some more money and get the more expensive 'hot mirrors', a glass with a multi-layer dielectric coating that reflects infrared radiation, while allowing visible light to pass through. But even these didn't satisfy our needs, so only the combination of both in front of each light made it possible for us to deal with the enormous heat input. Figure A.1 shows a photograph of one of our lights with the 'glasses'.

Figure A.1: 750 Watts theater light with hot mirror and heat absorbing glass for reduced heat output.

Apart from those filters, we also blocked most of the light with metal shields, which were put on the outside of our tank and held by magnets glued onto the plexiglas. This allowed an easy and quick way for manipulating the size of the volume illuminated.

Another tricky part was the driving mechanism, since our stepper motor had little problems lifting the weight of the connection rod plus shaft housing plus shaft plus sphere, resulting in non-regular motion. So we balanced the weight by attaching springs to the shaft housing, so that the motor only had to accelerate the mass back and forth. These together with the linear rail, the shaft housing sliding on it, the eccentric connection rod and the disc are shown on the photograph in figure A.2.

Figure A.2: Photograph of the driving mechanism.

The liquid itself proved to be one of the hardest elements of the whole experiment. First of all, the right mixture of approx. 25 l had to be created with water and glycerol at a certain ratio (to give the desired viscosity and thus Re-number-regime) with the help of a scale that could only handle a maximum of 1 kg. So the whole procedure of getting the mixture took almost 2 hours. Then, the two fluids had to be mixed, which is not too hard but requires a considerable amount of shaking. The result is a medium-well mixed liquid with millions of tiny little bubbles that make it impossible to take any data for about 24 hours, the time it takes for them to vanish again. One problem there is that at the high viscosities we had to use (more than 90% of glycerol, leading to $\eta \approx 300\ mPas$ or $\nu \approx 240\ cSt$, see also figures A.3), the bubbles, although much lighter than the solution, are slowed down in their rising by their size as well as the extreme values of viscosity. This can be supported (and slightly sped up) by heating up the fluid with an immersion heater, which decreases the viscosity and makes it easier for the bubbles to rise. Unfortunately, heating up the fluid also decreases the solubility of gas in the liquid and thus also creates new bubbles. But these then can also rise faster, and after turning off the heater, the rest of the bubbles vanishes due to the increasing solubility of gas again.

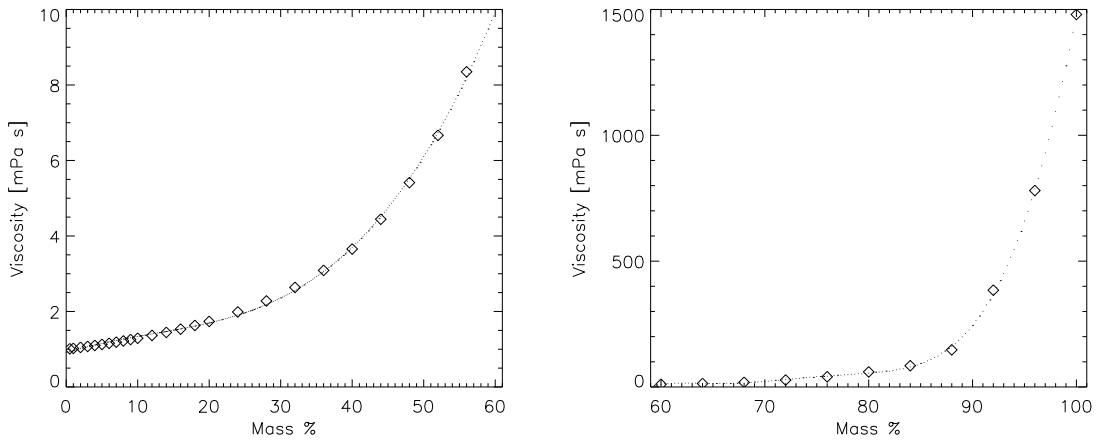

Figure A.3: Viscosity of glycerol as a function of mass %.

The strong temperature dependance of glycerol adds to the difficulties as well (see figure A.4). During the process of taking about 10 sequences in a row for example (depending on the frequency and number of phases of course, but typically something like several hours), the temperature rose by about 3° C - 4° C. This means a drop in the viscosity by 10% to 15%. Although one can compensate for this by decreasing the frequency to still get the same Re, it nevertheless is an annoying side-effect. The cooling of the tank afterwards takes again several hours (usually over night). Also, with such a high glycerol concentration, the mixture is hydrophilic, meaning that after sitting still for one night, the liquid would have a lower viscosity with an almost phase separated water enriched part on the top. This additional water can of course be stirred in, but the lower viscosity remains. Because of these problems, we installed a viscometer[1] and measured the viscosity for each single run.
At the beginning, we also had to fight bacteria, that consider the water/glycerol mixture an ideal agars. Adding chlorine bleach to the solution (approx. 50 ml in 20 l) got rid of that problem. Yet the soiling of the liquid over time is inevitable. We even had a removable lid with a hole for the shaft, but still, the dust and dirt would find a way to end up in the tank anyway. We had planned to run the experiment at much lower viscosities in the beginning, and installed a filtering system with a pump, but as soon as we had to go to values of $\nu > 90\ cSt$, the pump quit the service. So we had to exchange the liquid from time to time in order to get it clean again.

[1]Cannon-Fenske type using the tank itself as a temperature bath

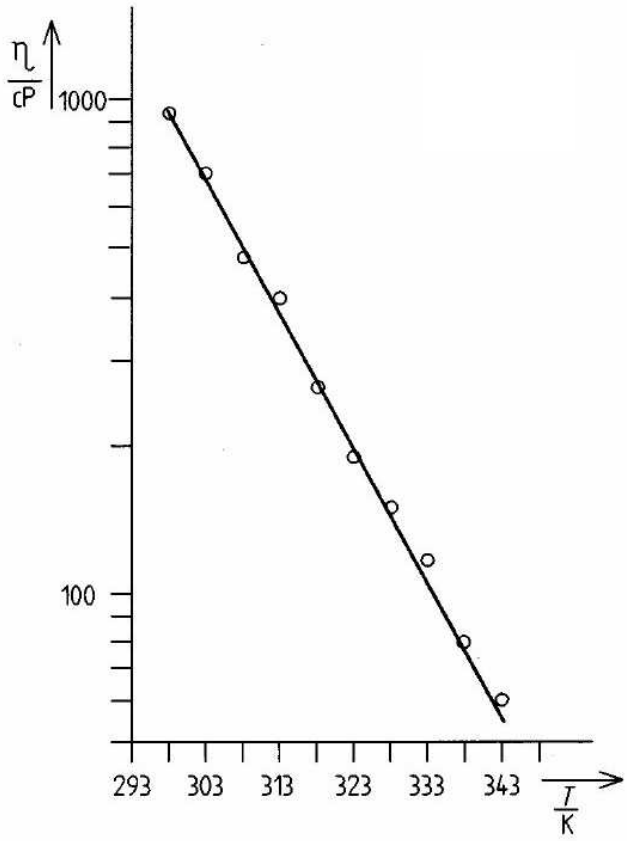

Figure A.4: Viscosity of glycerol as a function of temperature.

Appendix B

Computer programs and data structure

In this section, I want to give some more details about how the computer programs we mainly used to process the data work, and what this data looks like. The codes were all written in IDL [1], which is probably not the most efficient and fastest way to go, but combines data processing and analysis with a diversity of visualization tools. Let me first introduce the program that does the first step, i.e. taking the .tif-images from the cameras one by one, and extract features (= bright spots), called 'pt.pro'. It was written by Wolfgang Losert[2] and modified and extended ('htrack.pro', graphical interface to determine parameters) by Greg Voth. What it does is, it filters the image with a bandpass and then looks for maxima of intensity that are a minimum separation apart, have a minimum peak intensity and a minimum integrated intensity and then finally extracts the centroid of all these bright spots. This first step is very important and has to be done very carefully, since depending on the parameters chosen for running it, it will return any number of features from 0 to several thousand. The problem is that we cannot handle more than 200-400 particles, because we only have two cameras; on the other hand, taking a too small number will result in zero matches, since by no means do the brightest features have to be the same in the two different camera views. It also means a huge improvement regarding the size of the data: from 1 MB per frame (.tif-image) one goes to approx. 10 kB. This information (x_{2D}, y_{2D}, radius r, eccentricity ecc, integrated intensity int) is then passed on to the next program, 'idpart.pro'. This program was written by myself and does the matching, described in detail in subsection 3.1.1, using our mathematical model. After that, the output looks like this: (x_{3D}, y_{3D}, z_{3D}, x^A_{2D}, y^A_{2D}, x^B_{2D}, y^B_{2D}, r_A, r_B, ecc_A, ecc_B, int_A, int_B, ε_1, ε_2, frame #, time), a 17 x n matrix, where n is the number of matches found for each single frame. After combining all the data (3200 frames) from one sequence (17 x (n $\cdot$ 3200) matrix, a file of approx. 20 MB), it is ready to be put in the tracking program ('track.pro', written by John C. Crocker, David Grier and Eric R. Weeks[3], part of their "Particle tracking using IDL" package). That code 'constructs n-dimensional trajectories from a scrambled list of particle coordinates determined at discrete times, e.g. in consecutive video frames' (description from program comment). So now the particles each have a track ID, but unfortunately these tracks are

[1] ©Research Systems, Inc.

[2] (1999) see http://www.haverford.edu/physics-astro/Gollub/losert.html

[3] see http://www.physics.emory.edu/∼weeks/idl/

broken very often, since particles can disappear out the observation volume, be hidden in one camera's view, get lost in the matching or in 'pt.pro'. Nevertheless there are also many tracks that are hundreds of frames long, and the number of broken tracks could be reduced very efficiently by using a lower particle number density in the fluid (or by using more cameras), but on the other hand we also had to look for a higher number density in order to get enough data with a reasonable number of sequences. So there is always a certain trade-off between ideal theoretical conditions and the practical accomplishment. Finally, 'vel_fit.pro' (written by G. Voth) fits the tracks with polynomials (in our case of order 3), and then calculates velocities according to $\Delta v = \Delta\vec{x}/\Delta t$. The final result is a matrix with 26 columns, containing the information already given above plus (..., track ID, velocity flag, v_x, v_y, v_z, σ_{v_x}, σ_{v_y}, σ_{v_z}, $|\vec{v}|$). From there on, one can do several things, e.g. the statistical analysis suggested in subsection 3.5 (make a grid of bins to get velocity fields; requires a lot of data), or separate into phases (if there are more than one). In any case, one has to keep track of a lot of information, and samples at each step have to be taken to verify what the computer spits out. Apart from that, the data (especially for the 2 spheres) is fundamentally hard to visualize, since one has 3 coordinates plus 3 velocity components.

All in all, more than 1 Terabyte of data has been produced by this experiment and the analysis; a gigantic amount, especially regarding the backup and medium term storage. Even with a DVD-burner in each of the camera computers this task was and is a hard one, since the capacity of 4.5 GB on one medium is not a very efficient way to do this. A really nice thing for this kind of experiments would be a capturing hardware capable of pre-processing the images (the part done by 'pt.pro' in our case) to scale down the size of the raw data immediately during data acquisition. This problem will persist in the future, even with the size of hard-disks growing very fast, since both the camera resolutions and the frame rates will also keep on increasing.

Bibliography

[1] B.A. Grzybowski, H.A. Stone, G.M. Whitesides: *Dynamic self-assembly of magnetized, millimetre-sized objects rotating at a liquid-air interface*; Nature, Vol. 405, 1033-1036 (2000)

[2] S.-Y. Yeh, M. Seul & B. I. Shraiman: *Assembly of ordered colloidal aggregates by electric-field-induced fluid flow*; Nature, Vol. **386**, 57-59, 6 March 1997

[3] Greg A. Voth, B. Bigger, M.R. Buckley, W. Losert , M.P. Brenner, H.A. Stone, J.P. Gollub: *Ordered clusters and dynamical states of particles in a vibrated fluid*; Physical Review Letters **88**, 234301 (2002)

[4] Lord Rayleigh: *On the circulation of air observed in Kundt's tubes and some allied acoustical problems*; Philos. Trans. R. Soc. London Ser. A 175:1-21 (1883)

[5] H. Schlichting: *Berechnung ebener periodischer Grenzschichtströmungen*; Physikalische Zeit **33**, 327-335, 1932

[6] Van Dyke, M.: *An album of fluid motion*; The Parabolic Press, Stanford, California (1982)

[7] N. Riley: *Steady Streaming*; Annual Review of Fluid Mechanics (2001), 33:43-65

[8] D. Haydock, J.M. Yeomans: *Lattice Boltzmann simulations of the attenuation driven acoustic streaming*; Journal of Physics A: Mathematical and General **36** (2003) 5683-5694

[9] B.J. Davidson, N. Riley: *Cavitation microstreaming*; Journal of Sound and Vibration **15** (2), 217-233, 1971

[10] H. Zhao, S.S. Sadhal, E.H. Trinh: *Internal circulation in a drop in an acoustic field*; Journal of the Acoustical Society of America, Vol. 106, Number 6, 3289-3295, December 1999

[11] B.J. Davidson: *Heat transfer from a vibrating cylinder*; International Journal of Heat and Mass Transfer 1973, **16**:1703-27

[12] S.K. Chung, E.H. Trinh: *Containerless protein growth in rotating levitated drops*; Journal of Crystal Growth, 1998 **194**, 384-397

[13] P. Marmottant & S. Hilgenfeldt: *Controlled vesicle deformation and lysis by single oscillating bubbles*; Nature, Vol. **423**, 153-156, 8 May 2003

[14] N. Riley: *On a sphere oscillating in a viscous fluid*; Quarterly Journal of Mechanics and Applied Mathematics (1966), Vol. XIX, Pt. 4

[15] N. Riley: *Oscillatory viscous flows. Review and extension*; Journal of the Institute of Mathematics and its Applications (1967) **3**, 419-434

[16] L.D. Landau, E.M. Lifschitz: *Lehrbuch der theoretischen Physik, Band VI, Hydrodynamik*; 5. Auflage, Akademie Verlag, Berlin (1991)

[17] W.P. Raney, J.C. Corelli, P.J. Westervelt: *Acoustical Streaming in the Vicinity of a Cylinder*; Journal of the Acoustical Society of America, Vol. 26, Number 6, November 1954

[18] J.M. Andres, U. Ingard: *Acoustic Streaming at High Reynolds Numbers*; Journal of the Acoustical Society of America, Vol. 25, Number 5, 928-932, September 1953

[19] J.M. Andres, U. Ingard: *Acoustic Streaming at Low Reynolds Numbers*; Journal of the Acoustical Society of America, Vol. 25, Number 5, 932-938, September 1953

[20] J. Holtsmark, I. Johnsen, T. Sikkeland, S. Skavlem: *Boundary Layer Flow Near a Cylindrical Obstacle in an Oscillating, Incompressible Fluid*; Journal of the Acoustical Society of America, Vol. 26, Number 1, 26-39, January 1954

[21] H. Lamb: *Hydrodynamics*; 6th edition, Cambridge University Press, 1932

[22] C.-Y. Wang: *The flow field induced by an oscillating sphere*; Journal of Sound and Vibration **2**, (3), 257-269 (1965)

[23] H.M. Blackburn: *Mass and momentum transport from a sphere in steady and oscillatory flows*; Physics of fluids, Vol. 14, No. 11, (November 2002)

[24] T. Dracos (ed.): *Three-Dimensional Velocity and Vorticity Measuring and Image Analysis Techniques*; Kluwer Academic Publishers, Netherlands (1996)

[25] J. Mann, S. Ott and J.S. Andersen: *Experimental Study of Relative, Turbulent Diffusion*; Risø National Laboratory, Roskilde, Denmark, August (1999)

[26] H.F. Davis, A.D. Snider: *Introduction to Vector Analysis*; 6th edition, McGraw-Hill Professional Publishing (1990)

[27] PHYWE: *PHYWE series of publications · Laboratory Experiments · Physics*, 37070 Göttingen, Germany

[28] D. R. Lide (ed.): *CRC Handbook of Chemistry and Physics*; 82nd edition, CRC Press (2001)

Layout

[29] A. Diller: *LaTeX Line by Line*; second edition, Chichester (1999)

[30] M. Goossens, S. Rahtz, F. Mittelbach: *The LaTeX Graphics Companion*, Addison-Wesley (2001)

[31] K. Günther: *LaTeX GE-PACKT*; 1. Auflage, mitp-Verlag, Bonn (2002)

[32] H. Kopka: *LaTeX Band1 - Einführung*; 2. Auflage, Addison-Wesley, Bonn (1996)

[33] Schmidt, Knappen, Partl, Hyna: *LaTeX2e - Kurzbeschreibung*; Version 2, Regensburg (1998)

[34] N. Schwarz: *Einführung in TEX*; 3. Auflage, Addison-Wesley, Bonn, München (1991)

Thanks

Many people have contributed to the development of this thesis, be it directly or indirectly by their advice and support.

First of all, I have to thank my advisor at Wesleyan University, Prof. Dr. Greg Voth. Not only was he a technically excellent counselor, but with his positive way of thinking and his constantly friendly and helpful attitude a real pleasure to work with.

Next I want to emphasize that without the readiness of Prof. Dr. Wilfried Schoepe and Prof. Dr. Dietmar Göritz, who both (separately and after one another) agreed without hesitance to do the gradeing, this would not even have been a thesis at the university of Regensburg. In addition, Prof. Göritz immediately gave me a 'home' on my return to Regensburg in the form of an office, although technically, regarding my subject, I was a complete stranger to his group.

On the theoretical side of my experiment, a big thank you goes to Prof. Dr. Michael Brenner, who helped us resolve some of the issues with the discrepancies of the different approaches.

The analysis of the data would have been a lot harder if not impossible in the short period of time we had without the already existing computer programs written by Wolfgang Loser, John C. Crocker and Eric R. Weeks.

I also want to acknowledge the outstanding work of the AAA ('Akademisches Auslandsamt') at Regensburg, who do not stop trying until everybody that gets in touch with them has his place in one of the numerous exchange programs.

A whole bunch of people at Wesleyan University made my one-year-stay there a real pleasure and a great experience: Above all, I want to thank Marina Melendez and Barbara Schukoske at the graduate student office for their comprehensive and professional, yet always friendly support from the very first day. The same thing holds for the whole physics department, whose members made us (me and the other exchange students) feel fully integrated also from the very beginning.

Among the students, I really enjoyed the company of my two office-mates Andi ('... der Spiegel tittelt...') and Jon-from-Maine, who gave me hours of fun and great discussions about 'life' and physics, Holger, who almost became a real Bavarian in America, my lab-mate John, who had to cope with me occupying the camera equipment most of the year and still didn't lose his humor, Marcus ('Daaahh'), Josh and Thomas for the great fun during the 'Middletown-is-dead-and-empty'-period of the summer, watching all bad movies we could get and thus helping me survive after everybody else had gone home, and the machinists in the basement (Dave, Bruce and Tom) for their great work and funny discussions.

I also want to thank the 'AG Göritz', where I did most of the writing, for the friendly inclusion and the nice atmosphere during the last few months, and some quite helpful discussions on *TEX*-nical issues, especially my office-mate Gerald Schneider.

Another very important source of support for me were all my friends in Germany, who did not forget about me over the 12 months.

But my biggest thanks goes to my parents for their endless love and support during my whole life, and my brother and the rest of the family who make me know where I belong and feel 'at home'.

Statement

I hereby state that I produced this thesis myself and that I did not use any means other than the ones quoted above.
[Hiermit erkläre ich, dass ich die Diplomarbeit selbstständig angefertigt und keine Hilfsmittel außer den in der Arbeit angegebenen benutzt habe.]

Regensburg, den 12. März 2003

.....
(Florian Otto)